



The 2006–2007 Kuril Islands great earthquake sequence

Thorne Lay,¹ Hiroo Kanamori,² Charles J. Ammon,³ Alexander R. Hutko,⁴
Kevin Furlong,³ and Luis Rivera⁵

Received 30 December 2008; revised 12 June 2009; accepted 18 August 2009; published 24 November 2009.

[1] The southwestern half of a ~ 500 km long seismic gap in the central Kuril Island arc subduction zone experienced two great earthquakes with extensive preshock and aftershock sequences in late 2006 to early 2007. The nature of seismic coupling in the gap had been uncertain due to the limited historical record of prior large events and the presence of distinctive upper plate, trench and outer rise structures relative to adjacent regions along the arc that have experienced repeated great interplate earthquakes in the last few centuries. The intraplate region seaward of the seismic gap had several shallow compressional events during the preceding decades (notably an M_S 7.2 event on 16 March 1963), leading to speculation that the interplate fault was seismically coupled. This issue was partly resolved by failure of the shallow portion of the interplate megathrust in an $M_W = 8.3$ thrust event on 15 November 2006. This event ruptured ~ 250 km along the seismic gap, just northeast of the great 1963 Kuril Island ($M_W = 8.5$) earthquake rupture zone. Within minutes of the thrust event, intense earthquake activity commenced beneath the outer wall of the trench seaward of the interplate rupture, with the larger events having normal-faulting mechanisms. An unusual double band of interplate and intraplate aftershocks developed. On 13 January 2007, an $M_W = 8.1$ extensional earthquake ruptured within the Pacific plate beneath the seaward edge of the Kuril trench. This event is the third largest normal-faulting earthquake seaward of a subduction zone on record, and its rupture zone extended to at least 33 km depth and paralleled most of the length of the 2006 rupture. The 13 January 2007 event produced stronger shaking in Japan than the larger thrust event, as a consequence of higher short-period energy radiation from the source. The great event aftershock sequences were dominated by the expected faulting geometries; thrust faulting for the 2006 rupture zone, and normal faulting for the 2007 rupture zone. A large intraplate compressional event occurred on 15 January 2009 ($M_W = 7.4$) near 45 km depth, below the rupture zone of the 2007 event and in the vicinity of the 16 March 1963 compressional event. The fault geometry, rupture process and slip distributions of the two great events are estimated using very broadband teleseismic body and surface wave observations. The occurrence of the thrust event in the shallowest portion of the interplate fault in a region with a paucity of large thrust events at greater depths suggests that the event removed most of the slip deficit on this portion of the interplate fault. This great earthquake doublet demonstrates the heightened seismic hazard posed by induced intraplate faulting following large interplate thrust events. Future seismic failure of the remainder of the seismic gap appears viable, with the northeastern region that has also experienced compressional activity seaward of the megathrust warranting particular attention.

Citation: Lay, T., H. Kanamori, C. J. Ammon, A. R. Hutko, K. Furlong, and L. Rivera (2009), The 2006–2007 Kuril Islands great earthquake sequence, *J. Geophys. Res.*, *114*, B11308, doi:10.1029/2008JB006280.

¹Department of Earth and Planetary Sciences, University of California, Santa Cruz, California, USA.

²Seismological Laboratory, California Institute of Technology, Pasadena, California, USA.

³Department of Geosciences, Pennsylvania State University, University Park, Pennsylvania, USA.

⁴U.S. Geological Survey, Denver, Colorado, USA.

⁵Institut de Physique du Globe de Strasbourg, Strasbourg, France.

1. Introduction

[2] In September and early October of 2006 several moderate size ($m_b \sim 6.6$) and many smaller thrust faulting earthquakes occurred near the trench east of the Kuril Islands (Figure 1). About 45 days later, on 15 November 2006, the shallow part of the megathrust failed in an M_W 8.3 (global centroid moment tensor (CMT) solution, available at <http://www.globalcmt.org/CMTsearch.html>) low-angle thrust-faulting earthquake (USGS-NEIC: 11:14:13.570 UTC,

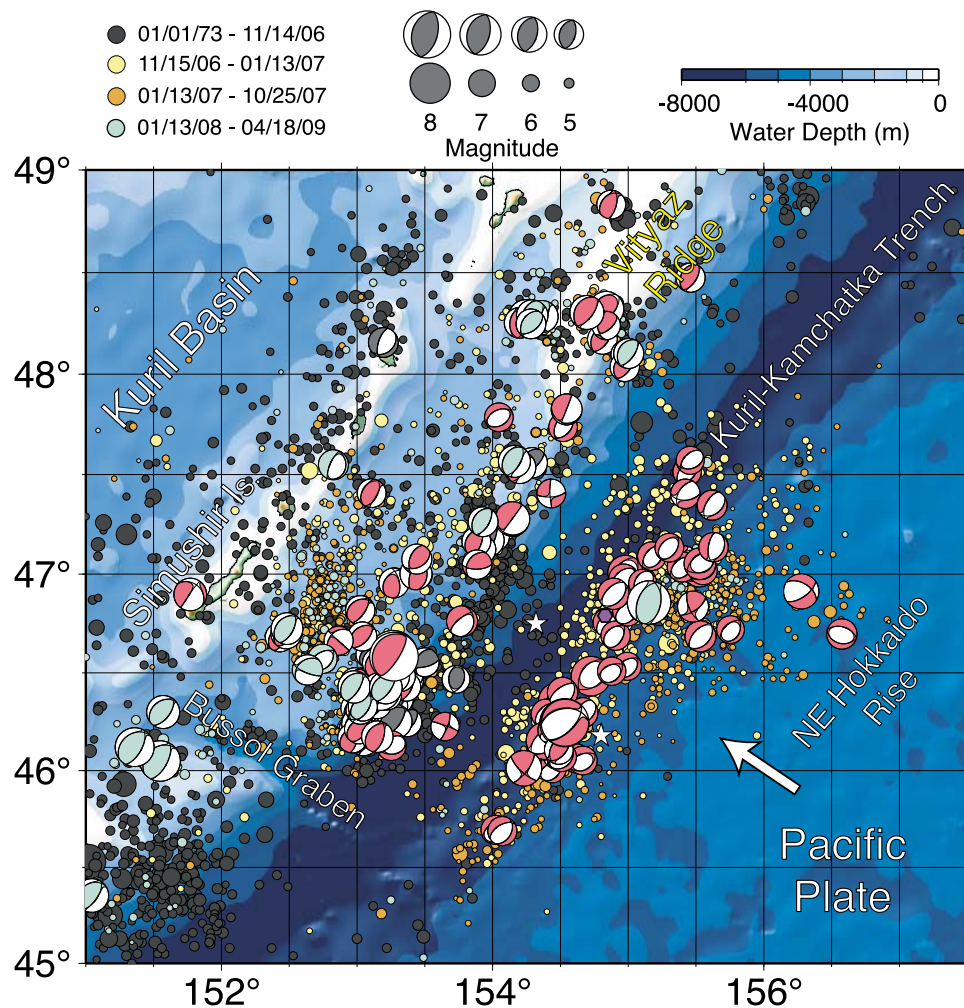


Figure 1. Map showing regional bathymetry and tectonic features, along with global centroid moment tensor (CMT) solutions for the larger earthquakes in the 2006–2007 Kuril Islands sequence (focal mechanisms), and NEIC epicenters of activity prior to the doublet (gray circles) between the two largest events (yellow circles), and following the 13 January 2007 event (orange circles). The gray shaded focal mechanisms are CMT solutions for foreshocks of the 15 November 2006 event, the red-shaded mechanisms occurred after the 15 November 2006 event, and events after 13 January 2008, including the trench slope 15 January 2009 event are green shaded. Focal mechanisms are plotted at the NEIC epicenters. The white stars indicate the CMT centroid locations for the two main shocks, which are shifted seaward relative to the NEIC locations. The arrow shows the estimated plate motion direction with a rate of 80 mm/yr computed using model NUVEL-1 [De Mets *et al.*, 1990] with North America fixed.

46.592°N 153.266°E, m_b 6.5, M_S 7.8 <http://neic.usgs.gov/neis/epic/epic.html>) that ruptured about 250 km northeastward along the trench strike. Intraplate activity beneath the outer trench wall began within minutes of the large megathrust event and continued for another two months until 13 January 2007, at which time an M_W 8.1 (CMT) normal-faulting earthquake (USGS-NEIC: 04:23:21.160 UTC, 46.243°N 154.524°E, m_b 7.3, M_S 8.2) ruptured ~200 km along a steeply dipping fault beneath the trench slope. This great earthquake sequence (Figure 2) partially filled a major seismic gap [Fedotov, 1965, 1968; Kelleher and McCann, 1976; McCann *et al.*, 1979; Lay *et al.*, 1982; Nishenko, 1991; Laverov *et al.*, 2006; Kulinich *et al.*, 2007] northeast of the great 1963 Kuril Islands (M_w = 8.5) earthquake [Kanamori, 1970; Beck and Ruff, 1987] and southwest of

the great 1952 Kamchatka (M_w = 9.0) earthquake [Kanamori, 1976; Johnson and Satake, 1999] (Figure 3).

[3] Moderate-amplitude tsunamis were produced around the Pacific by the two earthquakes [Rabinovich *et al.*, 2008; Tanioka *et al.*, 2008; Fujii and Satake, 2008; Baba *et al.*, 2009]. Observed tsunami heights at remote distances were less than 1.2 m for the 15 November 2006 event [Rabinovich *et al.*, 2008], except for a 1.76 m wave that destroyed two docks and damaged another in Crescent City, California [Kowalik *et al.*, 2008; Horrillo *et al.*, 2008]. Local tsunamis for the 2006 event are computed to have been from 2 to 4 m [Rabinovich *et al.*, 2008], but there are no local tide gauge recordings. Biological expeditions to the region have documented tsunami erosion effects on several islands of the central Kurils, with peak tsunami runups for

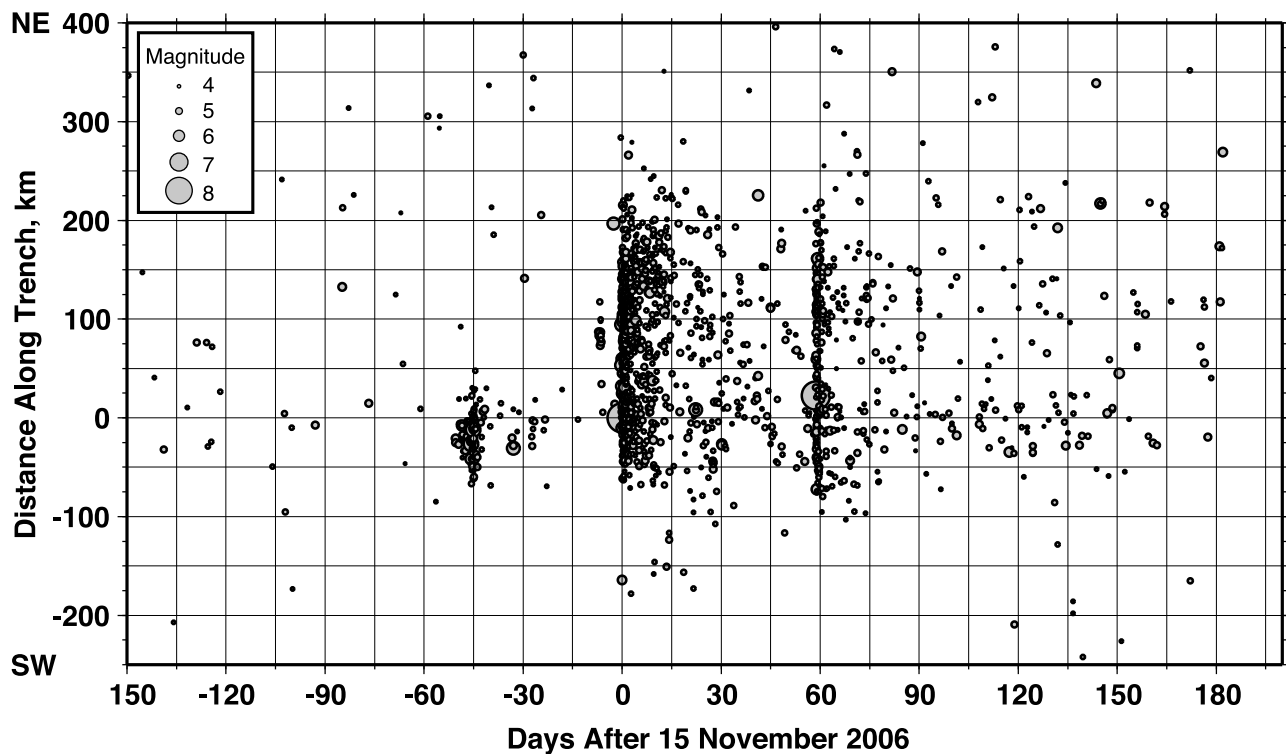


Figure 2. Space-time seismicity diagram showing the temporal evolution of the 2006–2007 Kuril Islands earthquake sequence along the trench (the 15 November 2006 earthquake origin time and hypocenter are used as the reference). The September foreshock sequence and the two main shock sequences are apparent and their spatial relationship is indicated in Figure 1.

the 15 November 2006 event of 15–20 m on Matua and Simushir islands [Levin *et al.*, 2008; MacInnes *et al.*, 2007]. Geomorphic evidence for prior large tsunami erosion events in the region supports the notion of strong seismic coupling in the gap [Pinegina *et al.*, 2007]. The presence of the Kuril Islands, particularly the now uninhabited Simushir Island (Figure 1, 46°N, 152°E) arcward of the 2006 rupture zone, appears to have prevented any large tsunami from penetrating into the Sea of Okhotsk to strike Sakhalin or the Russian mainland coast [Rabinovich *et al.*, 2008]. The 13 January 2007 event produced remote tsunami waves less than half the amplitude of the thrust event in most locations, and only 0.37 m high in Crescent City. However, the ground shaking in Japan produced by the January event was significantly stronger than for the November event, consistent with the larger m_b and M_S for shorter period seismic waves for the 2007 event.

[4] Given the timing and proximity of the two events, it is clear that the January event can be described as an aftershock broadly speaking, but one of unusually large size, qualifying these events as a doublet [Lay and Kanamori, 1980; Kagan and Jackson, 1999; Ammon *et al.*, 2008]. In

this instance, the doublet involves rupture of distinct faults with different focal mechanisms. Activation of moderate size intraplate seismicity seaward of large interplate thrust events has commonly been observed [e.g., Christensen and Ruff, 1988], but the seismic hazard associated with such trench slope–outer rise aftershock activity has not been considered in detail. Given the characteristically high stress drop and strong short-period seismic wave excitation for intraplate events, this large Kuril doublet provides a demonstration of the hazard presented by triggering of rare, very large outer rise intraplate events. This intriguing great earthquake sequence also presents an opportunity to examine subduction zone earthquake processes including the relationship of structure and strain accumulation in the upper and lower plates with coseismic slip on the megathrust, large-earthquake interactions within the subducting plate, and stress release and the nature of faulting seaward of the megathrust.

[5] Because of its location in the trench slope–outer rise region, the 13 January 2007 earthquake might conventionally be viewed as a flexural plate-bending event, a perspective that may be enhanced by the occurrence of a relatively deep

Figure 3. Shallow seismicity distribution (NEIC epicenters) and all CMT solutions for events along the central Kuril Island region prior to the 15 November 2006 event. CMT centroid locations have an overall location bias somewhat toward the southeast. The approximate aftershock zones of the great 1963 Kuril Islands ($M_w = 8.5$) and 1952 Kamchatka ($M_w = 9.0$) earthquakes are outlined in red, and the epicenter of the 1915 ($M_S 8.0$) event is shown by a red asterisk. The along-strike extent of the 2006–2007 great doublet is shown by the dashed red line with arrowheads. Outer rise activity of extensional or compressional nature is highlighted. The outer rise compressional mechanisms in red are from Christensen and Ruff [1988] with the 16 March 1963 event being labeled.

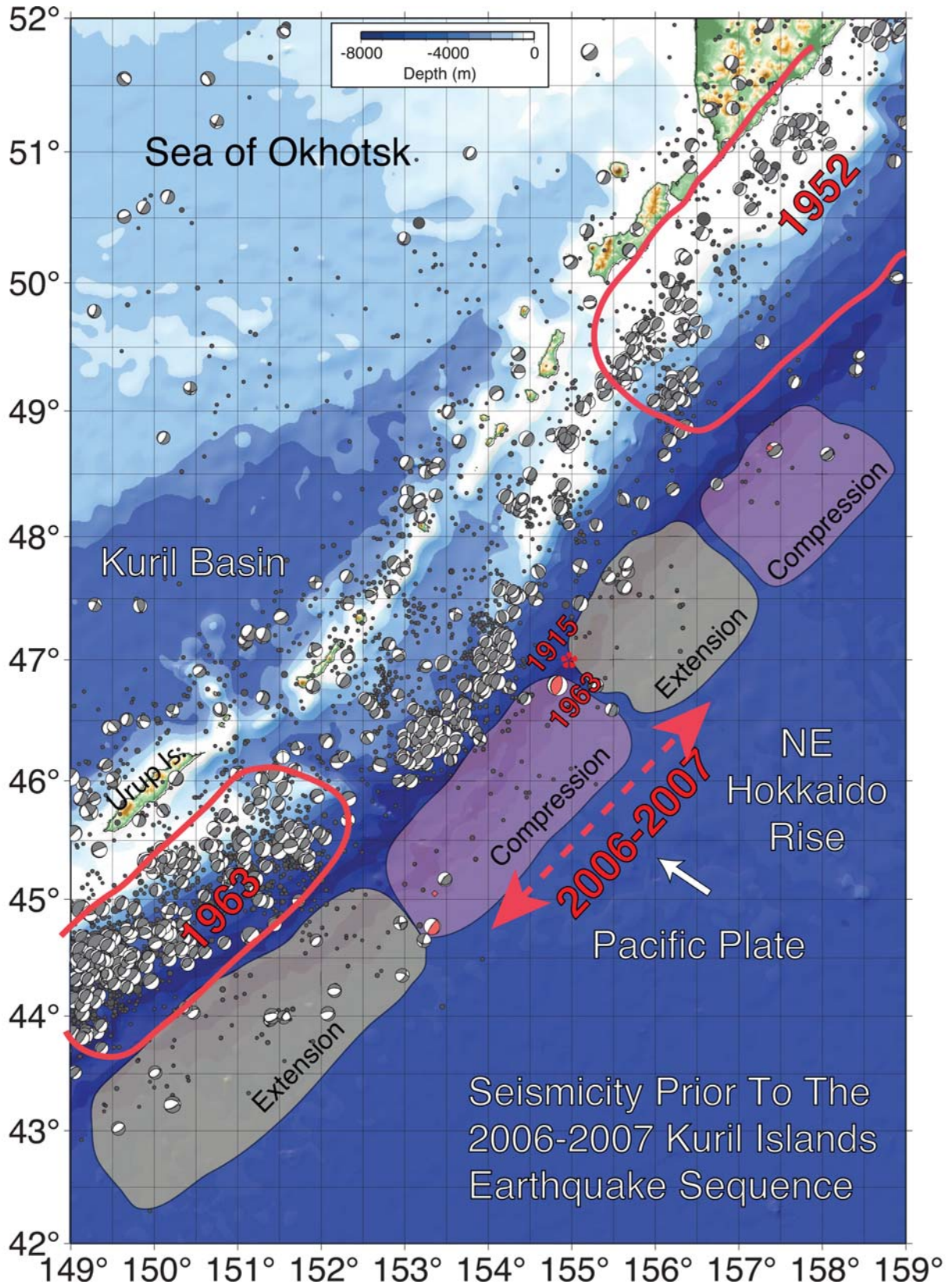


Figure 3

(~45 km) trench slope compressional event (Figure 1) on 15 January 2009 (USGS-NEIC: 17:49:39.0 UTC, 46.857°N 155.154°E, m_b 6.9, M_S 7.5). While there is no question that the slab must bend and deform as it approaches the subduction zone, such a large normal faulting event being triggered by a nearby large thrust event warrants consideration of the specific intraplate deformation of this sequence for the following reasons: (1) the event occurred beneath the outer trench slope, not in the outer rise per se, where flexural bending is concentrated, and such large normal-faulting trench slope events have not been recorded elsewhere along the Kuril arc; (2) the 2007 rupture appears to have extended to about 33 km depth, indicating a flexural bending neutral stress surface >33 km deep, and an elastic thickness >66 km, larger than expected for the approximately 100 Ma age of the subducting lithosphere; (3) the normal faulting event was preceded by a somewhat deeper 1963 intraplate compressional faulting earthquake in approximately the same location, suggesting very large temporal modulation of the stress in the plate by the interplate stress cycle; and (4) the January 2009 compressional event occurred near the 1963 compressional event, also at larger depth than the 2007 normal faulting event. The combination of the earthquake history in the region, quantification of the amount of interplate slip and the intraplate lengthening found below, and the overall size of the 13 January 2007 earthquake rupture imply direct linkage of strain accumulation and release between the doublet events during the stress cycle. This perspective emphasizes the distinct nature of rare great normal-faulting events at trenches, which have long been characterized as ‘plate decoupling’ events rather than bending events [Kanamori, 1971]. By comprehensively quantifying the rupture process of this great doublet, we seek to shed light on the stress system in the subducting slab near the trench.

[6] The 2006–2007 Kuril Island great doublet events were globally recorded by a large number of broadband seismic stations. In the following, we analyze this complicated great earthquake sequence and estimate the slip distributions and other source properties of the two main shocks using surface and body wave signals that span a broad range of frequencies and resolve distinct aspects of the rupture processes. We extend results of an initial investigation of the sequence [Ammon *et al.*, 2008], using additional methodologies and enhanced procedures to characterize the rupture processes, progressing from overall point source characterizations to first-order directivity estimates to finite fault solutions. We then consider the nature of stress interactions between the doublet events and other large events in the region, exploiting the unique opportunity provided by this unusual seismic doublet.

2. Tectonic Setting

[7] Seismic activity and regional tectonic structures in the immediate vicinity of the 2006–2007 Kuril Islands sequence are illustrated in Figure 1. In this region, the Pacific plate subducts at a rate of ~80 mm/yr (NUVEL-1 [De Mets *et al.*, 1990]) beneath the North American plate (or a separate Sea of Okhotsk microplate) toward a direction of ~N60°W. The plate kinematic framework of the region is discussed in detail by Apel *et al.* [2006]. The Pacific plate

lithospheric age at the subduction zone is somewhat uncertain because it formed during the Cretaceous quiet period, but is about 100–120 Ma. There is moderate bathymetric relief on the Pacific plate in the Northeast Hokkaido rise along the central Kuril island arc, but no profound change in the subducting plate structure [Kelleher and McCann, 1976]. However, the Vityaz Ridge along which the island arc is distributed is significantly disrupted in the source region of the great doublet (Figure 1). The sequence is bordered on the southwest by a substantial seafloor canyon called the Bussol graben (near 46°N, 152.5°E), and on the northwest by a ~2 km deep fore-arc basin with inclined blocks extending to about 48°N, 154°E, near the northeastern limit of the 2006 rupture zone, where the Vityaz Ridge resumes [Laverov *et al.*, 2006; Kulinich *et al.*, 2007]. The source region is located seaward of the tapered northern end of the obliquely spread Kuril back-arc basin (Figure 1), which is underlain by thin oceanic crust, whereas surrounding regions under the Sea of Okhotsk have thicker (~20 km) submerged continental margin crust [Zheng and Lay, 2006].

[8] The regional distribution of shallow seismicity along the Kuril island arc prior to the 2006–2007 sequence is shown in Figure 3. Best double-couple mechanisms for CMT solutions from 1976 to 2006 are shown, along with a few additional solutions for earlier large outer rise events from Christensen and Ruff [1988]. Aftershock zones for the great 1963 Kuril ($M_w = 8.5$) and 1952 Kamchatka ($M_w = 9.0$) events are outlined. Note that background interplate seismicity defined by the CMT shallow thrust fault solutions shifts seaward in the vicinity of the 2006–2007 sequence, and appears to be confined to a markedly narrower zone of activity than along the 1963 and 1952 rupture zones. This seaward shift of seismicity in the seismic gap occurs along the fore-arc basin apparent in the bathymetry. There is a corresponding narrowing of the overall width of the trench depression and a general increase of the free air gravity anomaly along this stretch of the subduction zone [Song and Simons, 2003; Ammon *et al.*, 2008]. The last few decades of seismic activity seaward of the megathrust along the Kuril Islands arc primarily involved extensional faulting after and outboard of the earlier great interplate thrusts in 1963 and 1952, with the exception of several relatively rare compressional events, including a particularly large M_S 7.2 trench slope event on 16 March 1963 (46.79°N, 154.83°E, Figure 3) [Christensen and Ruff, 1988; Raeesi and Atakan, 2009]. Areas of trench slope–outer rise compressional and extensional zones are highlighted in Figure 3, with one compressional area located in the region of the 2006–2007 sequence and another located near the southwestern end of the 1952 rupture zone and northeastern end of the seismic gap. With a substantial portion of the seismic gap still having uncertain seismic coupling and outer rise compressional events occurring offshore of part of that region, the remaining portion of the Kuril seismic gap is an area of concern for future large events.

2.1. Central Kuril Seismic Gap

[9] The region between the great 1963 and 1952 thrust events, called the central Kuril seismic gap, has relatively uncertain seismic history [McCann *et al.*, 1979; Nishenko, 1991]. There was a great historical event in the vicinity of

29 June 1780, when a long-duration earthquake produced a 10–12 m tsunami on Urup Island (along the 1963 rupture zone, Figure 3) and tsunami reports on Kotoi and Simushir Islands (located within the central Kuril seismic gap) [e.g., *Solov'ev and Ferchev*, 1961; *Iida et al.*, 1967]. This event appears to have spanned the 1963 rupture zone [*Fukao and Furumoto*, 1979; *Lay et al.*, 1982; *Beck and Ruff*, 1987], but its northeastern rupture extent is uncertain. The 1780 event is viewed by some Russian investigators as the last major rupture of at least the southwestern portion of the central Kuril seismic gap [e.g., *Laverov et al.*, 2006; *Kulinich et al.*, 2007]. Two other large events occurred within the northeastern region of the 1963 rupture zone on 7 September 1918 (45.5°N, 151.5°E; $M = 8.25\text{--}8.3$) and 8 November 1918 (44.5°N, 151.5°E; $M = 7.75\text{--}7.9$) (magnitudes from *Geller and Kanamori* [1977]; see Figure S5 of *Ammon et al.* [2008]). The latter event is located very close to the trench, suggesting similarity to the 2006–2007 sequence, but the faulting geometry is not known. The first 1918 event was assigned a tsunami magnitude of 8.7 by *Abe* [1979] and produced a strong local tsunami of 12 m on the east coast of Urup Island [*Iida et al.*, 1967], similar to the 1780 event. *Beck and Ruff* [1987] reviewed the tsunami observations and inferred that the northeastern 2/3 of the 1963 rupture zone failed in the 1918 event. It is again unclear whether the event ruptured northeast of the Bussol graben, but some estimates of tsunami source area support this possibility [*Fedotov*, 1965; *Fukao and Furumoto*, 1979]. Portions of the 1963 rupture zone failed again in 1995 (M_w 7.9) and 1991 (M_w 7.6) [*Perez*, 2000], indicating a relatively short recurrence interval compared to the central Kuril gap region, even if the latter did partially rupture in 1918.

[10] An event on 1 May 1915 (47°N, 155°E), with magnitude values ranging from 7.7 to 8.1 [see *Geller and Kanamori*, 1977; *Pacheco and Sykes*, 1992] is unambiguously located within the central Kuril seismic gap (Figure 3). This event, along with the larger 1918 event, were invoked by *Fedotov* [1965, 1968], to characterize the region as a seismic gap with potential for future large earthquakes. The source area estimated from aftershocks for the 1915 event overlaps with the northeastern portion of the 2006–2007 sequence. The 1915 event was not accompanied by a large tsunami. It is not certain that this was an interplate rupture, as the epicentral location from *Gutenberg and Richter* [1954] (Figure 3) is located in the northeastern portion of the 2007 trench slope event aftershock zone.

2.2. Great Doublet Seismicity Sequence

[11] The seismicity time line in Figure 2 indicates the initial burst of moderate-size thrust events (gray solutions in Figure 1) that commenced in late September 2006 near the eventual hypocentral region of the 15 November 2006 great event. Waveform modeling of teleseismic P waves for thrust events in the hypocentral region indicates source depths of 10 to 12 km below the ocean bottom, implying a shallow interplate fault dip from the trench of $<15^\circ$. The great thrust event initiated vigorous activity that not only includes aftershocks along a 250 km long region of the interplate boundary, but comparable levels of simultaneous activity in the outer rise (yellow dots in Figure 1). The 13 January 2007 event occurred after a 2 month delay, and was followed by aftershocks (orange dots in Figure 1) that

overlap with the earlier trench slope activity, but are somewhat concentrated to the southeast of the earlier thrust-induced foreshock activity. The megathrust environment had continuing activity after the January event, indicating strong interactions between the two fault zones. The aftershock activity of the 15 November earthquake decreased substantially after two weeks, gradually decaying to a relatively low level over the next month (Figure 2). The 13 January aftershocks were less numerous in the first 2 weeks after the main shock compared with after the 15 November sequence.

3. First-Order Attributes of the Great Earthquakes

[12] We apply several procedures to characterize the overall geometry and extent of faulting before developing finite source rupture models for the two great Kuril events. Given the restriction to teleseismic observations of the faulting, and the intrinsically limited resolution of source processes provided by teleseismic signals, we first seek further constraints on the overall faulting orientation using point source inversion of very long-period signals and then perform short-period and long-period seismic wave directivity analysis to constrain the rupture velocity. These analyses, along with results from prior studies, then bound the parameter space for high-resolution body wave finite source inversions.

3.1. W Phase Inversion for Point Source Geometry

[13] The global CMT solutions for the two main shocks provide quite well constrained point source characterizations for body wave and/or surface wave ground motions (Tables 1 and 2), with long period waves (~ 200 s) being emphasized in the inversions because of the large seismic moment of the events (*M. Nettles*, personal communication, 2008). For very large earthquakes like these, it is possible that source finiteness effects can bias point source representations based on 200 s period waves, so we performed inversions of ground motions with periods between 200 and 1000 s from the P wave arrival until the large amplitude Rayleigh waves arrive. The very long period motions in this time window have been called the W phase [*Kanamori*, 1993], and are basically comprised of very long period, high group velocity spheroidal fundamental mode energy superimposed on body wave (or spheroidal overtone) arrivals. Large ruptures generate sufficient signal-to-noise ratios such that energy in this window can be stably inverted for a point source moment tensor, with accurate prediction of the excitation and propagation of these waveforms being provided by standard Earth models such as PREM [*Dziewonski and Anderson*, 1981]. Because the waveform interval precedes the large short-period Rayleigh wave arrivals, near real time inversion of the W phase can provide rapid characterization of the very long period source process for large events for use in tsunami warning systems [e.g., *Kanamori and Rivera*, 2008], but it is also an intrinsically robust and straightforward way to resolve overall faulting parameters for any large event. W phase inversion was performed for both main shocks.

[14] For the 15 November 2006 event, 28 broadband stations with stable ultralong-period (STS-1) seismometers

Table 1. Seismic Modeling Results for 15 November 2006

Modeler	ϕ (deg)	δ (deg)	λ (deg)	M_0 (N m)
GCMT	215	15	92	3.5×10^{21}
J. Polet (personal communication, 2007)	206	9	84	3.9×10^{21}
<i>W</i> phase, this study	221	21	97	2.4×10^{21}
Surface waves, this study	237	12	116	2.7×10^{21}
C. Ji (Rupture process of the 2006 NOV 15 magnitude 8.3 - KURIL Island earthquake (revised), 2006, available at http://earthquake.usgs.gov/eqcenter/eqinthenews/2006/usvcam/finite_fault.php)	220	15	var.	3.9×10^{21}
Y. Yagi (http://www.geo.tsukuba.ac.jp/press_HP/yagi/EQ/Chishima/ , 2006)	214	15	97	1.6×10^{21}
Y. Yamanaka (http://www.eri.u-tokyo.ac.jp/sanchu/Seismo_Note/2006/EIC183.html , 2006)	220	25	96	2.1×10^{21}
Ammon <i>et al.</i> [2008]	215	15	92	4.6×10^{21}
Steblov <i>et al.</i> [2008]	211	9–22	varies	5.1×10^{21}
Raeesi and Atakan [2009]	220	15	100	2.8×10^{21}
Baba <i>et al.</i> [2009]	220	10	varies	$5.0\text{--}5.3 \times 10^{21}$
<i>P</i> waves this study	220	15	96 average	5.0×10^{21}

with flat response to ground velocity out to ~ 360 s period at distances less than 50° from the source were used to invert for a point source moment tensor. We directly follow the procedures for recovering ground displacements and windowing the *W* phase as described by Kanamori and Rivera [2008]. The solution and fits to 13 of the stations are shown in Figure 4 (other stations used are YSS, ERM, MA2, INCN, SSE, MDW, ULN, TATO, COLA, ENH, WHY, QIZ, WMQ, KIP, ALE). The inverted moment tensor has a small intermediate eigenvalue (eigenvalues are 2.324, 0.072 and -2.396 in units of 10^{21} N m), and the best double couple nodal plane for shallow underthrusting has an orientation given by strike $\phi = 221^\circ$, dip $\delta = 21^\circ$, rake $\lambda = 97^\circ$. The estimated seismic moment $M_0 = 2.4 \times 10^{21}$ N m ($M_W = 8.2$). This is quite similar to the global CMT solution, for which the best double couple has orientation $\phi = 215^\circ$, $\delta = 15^\circ$, $\lambda = 92^\circ$ and $M_0 = 3.5 \times 10^{21}$ N m ($M_W = 8.3$). Comparison of the fits to the *W* phase data for the two solutions indicates slight improvements for the *W* phase inversion, and the strike for this solution is closer to the regional trend of the trench. Moment tensor inversion of intermediate period Rayleigh waves alone by J. Polet (personal communication, 2007) gave a best double couple solution with $\phi = 206^\circ$, $\delta = 9^\circ$ and $\lambda = 84^\circ$, with $M_0 = 3.9 \times 10^{21}$ N m ($M_W = 8.3$). As apparent in Figure 4, the solution from inversion of the *W* phase provides excellent predictions of the following Rayleigh wave arrival in the very long

period passband. Still, the dip is not well resolved, and there is direct trade-off with the seismic moment such that shallower estimates of dip result in larger estimates of seismic moment (and hence, larger M_W). Inversion of the Rayleigh wave arrivals at the same stations for the passband 0.001–0.01 Hz yielded a similar moment tensor with the best nodal planes being $\phi = 237^\circ$, $\delta = 12^\circ$, $\lambda = 116^\circ$, and a seismic moment estimate of 2.7×10^{21} N m ($M_W = 8.2$). Given the geometry of the subduction zone and the shallow depth of small events near the hypocenter mentioned above, we prefer a dip of 15° and a strike of about 220° , but view the slight differences between these long-period solutions as indicative of uncertainties ($\pm 15^\circ$ for strike; $\pm 6^\circ$ for dip) in any point source representation for the thrust event. The source parameter estimates for the 2006 event from various investigations are summarized in Table 1.

[15] Inversion of 22 *W* phase signals for the 13 January 2007 event (Figure 5; additional stations used are PET, YSS, ERM MIDW, SSE, TATO, ENH, KIP, WMQ) also yielded a solution with very small intermediate eigenvalue (eigenvalues are 1.637, 0.037, -1.674 in units of 10^{21} N m), and best double couple nodal planes with orientations $\phi = 217^\circ$, $\delta = 62^\circ$, $\lambda = -124^\circ$ (northwest dipping plane) and $\phi = 92^\circ$, $\delta = 43^\circ$, $\lambda = -43^\circ$ (south dipping plane) and $M_0 = 1.7 \times 10^{21}$ N m ($M_W = 8.1$). The CMT solution best double couple (Figure 5) has orientation $\phi = 266^\circ$, $\delta = 39^\circ$, $\lambda = -54^\circ$ (northwest dipping plane) and $\phi = 43^\circ$, $\delta = 59^\circ$ and $\lambda = -115^\circ$

Table 2. Seismic Modeling Results for 13 January 2007

Modeler	ϕ (deg)	δ (deg)	λ (deg)	M_0 (N m)
GCMT	43	59	-115	1.8×10^{21}
J. Polet (personal communication, 2007)	266	39	-54	
	248	41	-75	1.4×10^{21}
	48	51	-103	
<i>W</i> phase this study	92	43	-43	1.7×10^{21}
	217	62	-124	
Surface waves this study	34	56	-124	1.5×10^{21}
	264	47	-51	
C. Ji (Rupture process of the 2007 Jan 13 magnitude 8.1 - KURIL Island earthquake (revised), 2007, http://earthquake.usgs.gov/eqcenter/eqinthenews/2007/us2007xmae/finite_fault.php)	42	58	varies	1.9×10^{21}
Y. Yagi (http://www.geo.tsukuba.ac.jp/press_HP/yagi/EQ/2007Chishima/ , 2007)	215	45	-110	1.6×10^{21}
Y. Yamanaka (http://www.eri.u-tokyo.ac.jp/sanchu/Seismo_Note/2007/EIC184.html , 2007)	220	37	-108	2.7×10^{21}
Ammon <i>et al.</i> [2008]	43	59	-115	1.5×10^{21}
Steblov <i>et al.</i> [2008] (Geodetic)	43	59	-115	2.7×10^{21}
Raeesi and Atakan [2009]	40	45	-97	1.7×10^{21}
Body waves this study	43	59	-105	2.8×10^{21}
	220	47	-106	2.6×10^{21}

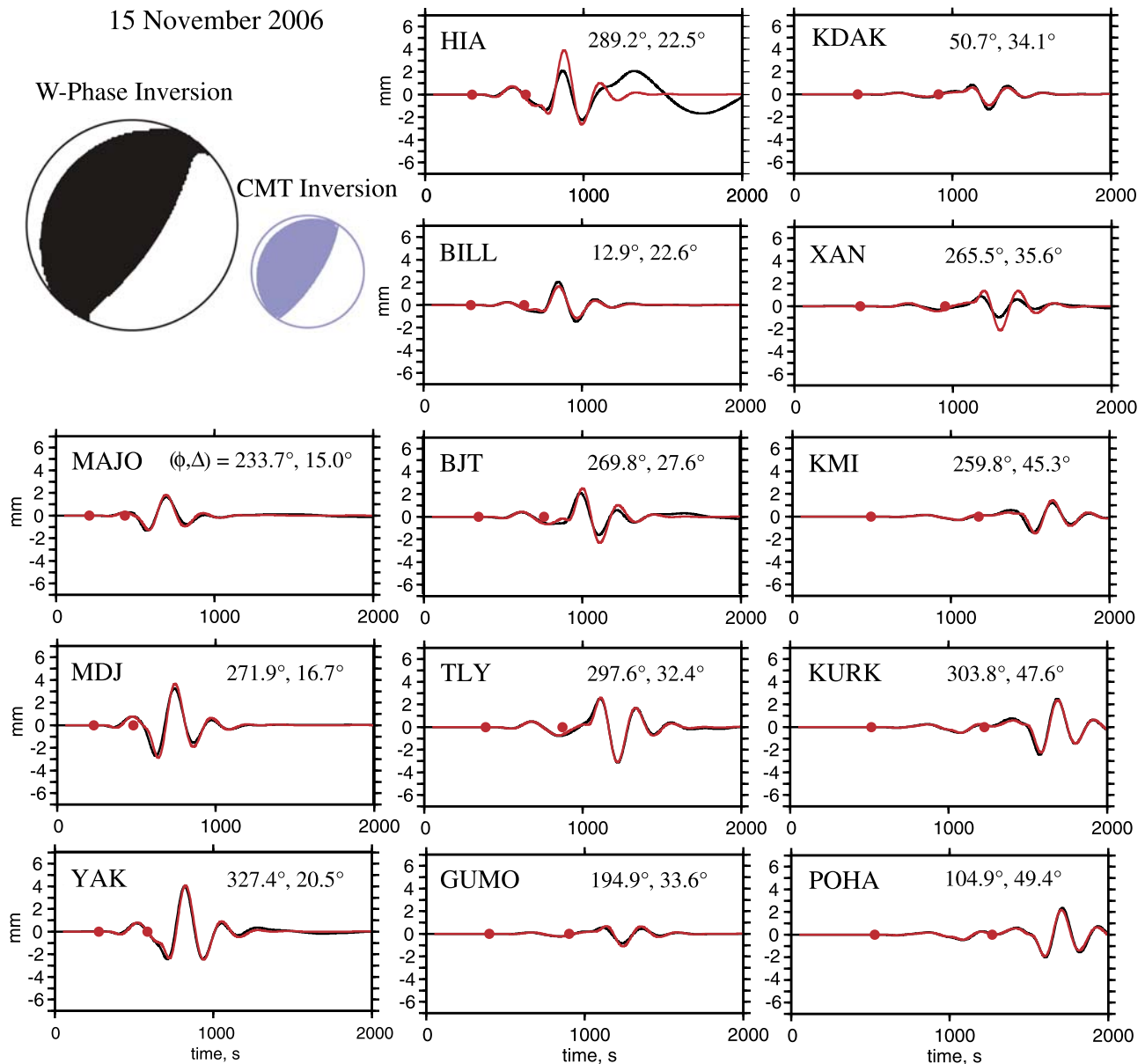


Figure 4. W phase waveform inversion results for the great thrust earthquake on 15 November 2006. Vertical ground motions band-pass filtered in the 0.001–0.005 Hz passband (black lines) are overlain by synthetics (red lines) computed for the W phase inversion for a point source moment tensor (black focal mechanism). The CMT solution is shown for comparison. The waveform segments used in the inversion are bounded by red dots, and correspond to very long period spheroidal fundamental mode and overtone energy. The station azimuths (ϕ) and epicentral distance (Δ) are indicated. All data are from distances less than 50° . This is about half of the data used in the inversion. The Rayleigh wave airy phase signal following the W phase segment is generally very well predicted by the W phase solution. Some stations, like HIA, have instrument problems during or after the Rayleigh wave arrival, but the W phase signal is uncontaminated.

(southeast dipping plane), with $M_0 = 1.8 \times 10^{21}$ N m ($M_W = 8.1$). Moment tensor inversion of the intermediate period fundamental mode Rayleigh waves alone (J. Polet, personal communication, 2007) had $\phi = 248^\circ$, $\delta = 41^\circ$, and $\lambda = -75^\circ$ (northwest dipping plane) and $\phi = 48^\circ$, $\delta = 51^\circ$, $\lambda = -103^\circ$ (southeast dipping plane), with $M_0 = 1.4 \times 10^{21}$ N m ($M_W = 8.1$). Comparison of synthetics for the various models suggests modest, but systematic differences for several stations, and the W phase signals are fit better overall

by the W phase solution. All three solutions have at least one nodal plane striking parallel to the trench and the trend of the seismicity, which is the likely fault geometry. The discrepancy between the W phase and CMT solutions (Figure 5) is larger for this event than for any of the other great earthquakes for which comparisons have been made [Kanamori and Rivera, 2008]. For the CMT solution, the southeast dipping plane strikes along the trench, but the northwest dipping plane is very oblique to the trench. The W phase solution has

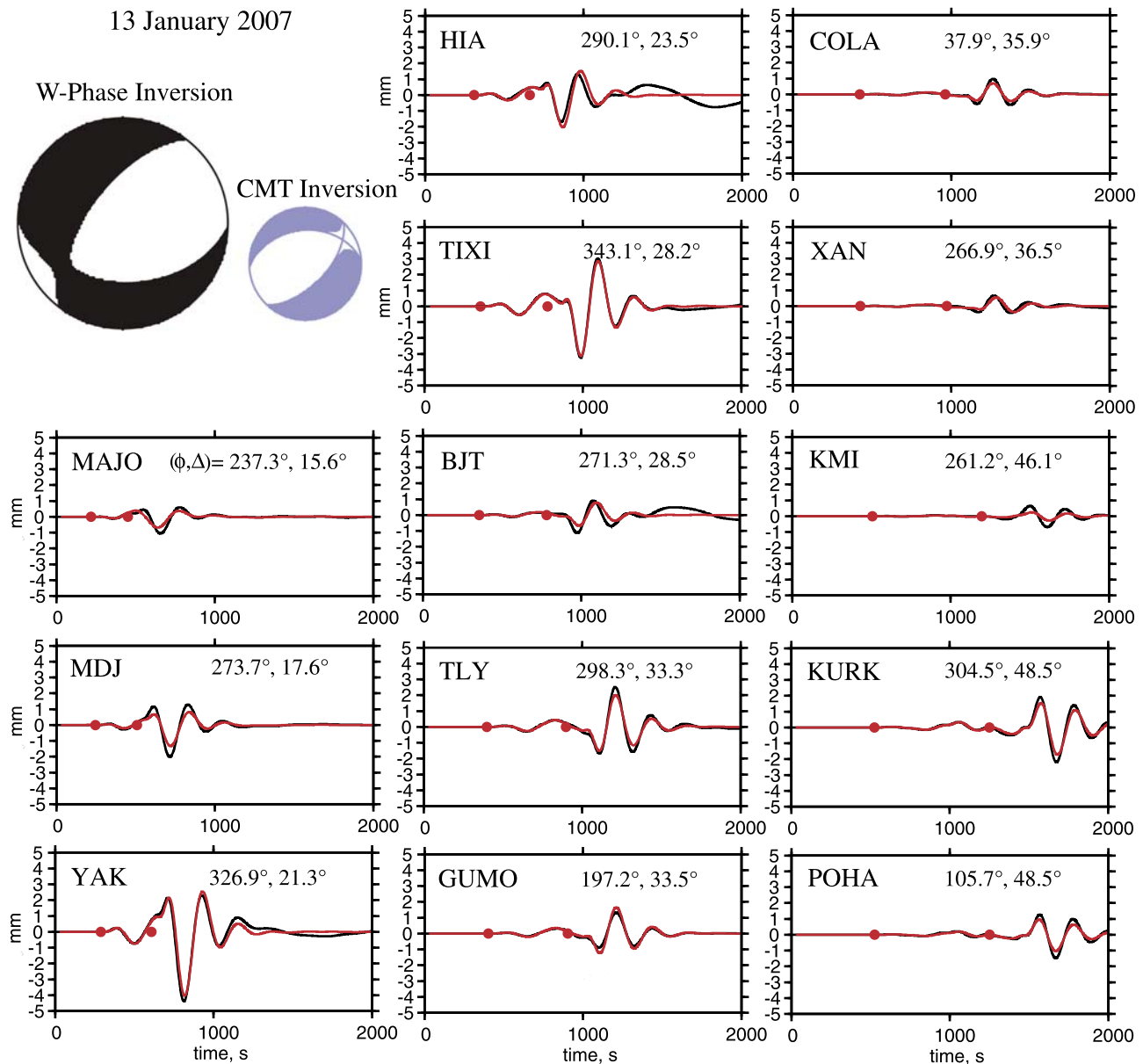


Figure 5. *W* phase waveform inversion results for the great normal-faulting earthquake on 13 January 2007. Vertical ground motions band-pass filtered in the 0.001–0.005 Hz passband (black lines) are overlain by synthetics (red lines) computed for the *W* phase inversion for a point source moment tensor (black focal mechanism). The CMT solution is shown for comparison. The waveform segments used in the inversion are bounded by red dots, and correspond to very long period spheroidal fundamental mode and overtone energy. The station azimuths (ϕ) and epicentral distance (Δ) are indicated. All data are from distances less than 50° . This is about half of the data used in the inversion. The Rayleigh wave airy phase signal following the *W* phase segment is slightly mispredicted by the *W* phase solution, suggesting some complexity in the long-period source process. Some stations, like HIA and BJT, have instrument problems during or after the Rayleigh wave arrival, but the *W* phase signal is uncontaminated.

just the opposite characteristic. The CMT centroid location is displaced seaward relative to the aftershocks, so there could be some effect on the solution. The *W* phase solution does vary slightly with centroid location, but remains distinct from the CMT solution for source locations along the aftershock zone. It is possible that there is complexity in the faulting process that is manifested in different moment tensors for different passbands; inversion of the surface wave signals for the same records (aside from 2 stations for which the

instrument went nonlinear during the Rayleigh wave arrival) gave a best double couple solution ($\phi = 34^\circ$, $\delta = 56^\circ$, $\lambda = -124$) very similar to the CMT solution. We have not ruled out the possibility that the location of this event near the Kuril trench, where there is steeply dipping bathymetry, causes biases in the solutions based on the 1D PREM Earth model Green functions, but it seems likely that the very long period *W* phase energy is less affected by structural effects than shorter period (~ 200 s) surface waves, particularly Love

waves. This uncertainty in the overall geometry leads us to obtain finite source models for both northwest dipping and southeast dipping nodal plane orientations. The preferred fault plane is not unambiguously resolved by master event aftershock relocations [Norimatsu and Mori, 2008]. Ideally, we will be able to discriminate between these two choices based on source directivity measures, or finite fault inversion preferences.

3.2. Short-Period P Wave Back Projection for Rupture Velocity

[16] We apply teleseismic short-period P wave back projection using a large aperture seismic network to image rupture front expansion for the two great events, with the primary goal being to bound the rupture velocity. Short period seismic energy is difficult to model quantitatively due to limitations of Earth models and typically spatially aliased sampling of the wavefield. However, short-period energy can resolve some aspects of overall rupture directivity of large earthquakes using azimuthally distributed stations [e.g., Ni *et al.*, 2005] or spatially dense seismic networks [e.g., Ishii *et al.*, 2005, 2007; Krüger and Ohrnberger, 2005]. This information can help to constrain lower frequency waveform inversions for which strong trade-offs exist between rupture velocity and spatial slip distribution.

[17] We back-projected teleseismic short-period signals recorded across a large network of broadband sensors in western North America at source-receiver distances of ~ 50 – 80° from the Kuril doublet events. A two-dimensional spatial grid at the surface encompassing the source region was defined, and differential travel time predictions for an assumed reference velocity model (IASP91; Kennett and Engdahl [1991]) were used to shift and sum all observations as though they originated at each grid point at corresponding rupture times. The change in travel time curve derivative ($dp/d\Delta$) and spatial distribution of the receivers yield space-time isolation of loci of coherent high frequency radiation from the fault from which average rupture velocity and source directivity can be measured and lower bounds for rupture length and duration estimated. This method provides very little depth resolution since relative differences of $dp/d\Delta$ do not vary significantly across tens of kilometers of depth.

[18] This short-period back projection method does not recover absolute slip, and is primarily sensitive to large and localized bursts of energy release rather than to energy released simultaneously over spatially extended rupture fronts, so the images only characterize limited aspects of the source radiation. However, rupture velocity can be inferred from the space-time pattern of any high frequency energy release bursts, and this is particularly difficult to resolve otherwise. Alignment of the short-period signals is important, and difficult, and time averaging over the stacked signals is needed to deal with both imprecise alignment of signals and the fact that the energy used is beyond the source corner frequency and intrinsically involves interference effects due to spatial and temporal finiteness. Station/path travel time statics for the emergent 15 November 2006 event were obtained by picking relative P wave arrival times for a large thrust event on 1 October 2006, located very close to the November epicenter, while the first arrivals

were directly aligned by cross correlation for the more impulsive 13 January 2007 event. The efficacy of the alignments for later arrivals is likely to degrade with spatial extent of the main shocks, but the rupture lengths are moderate, so this may not be severe. A 30 s time integration was applied in the final back projections in order to spatially isolate bursts of coherent short-period radiation received across the continental array.

[19] We use band-pass-filtered (0.8–2.0 Hz) P wave data from approximately 280 stations in North America for the 15 November 2006 event and approximately 350 stations for the 13 January 2007 event. Many of the stations are from the Transportable Array of EarthScope’s USArray. We also back-projected a smaller number (~ 70) of broadband stations located in Europe and in the Hi-Net array in Japan. The number and density of stations of Hi-Net is ideal for back projection applications for different regions such as the 2004 Sumatra [Ishii *et al.*, 2005] and 2005 Nias [Walker *et al.*, 2005] earthquakes, but the distances to the Kuril events span the upper mantle triplication range from ~ 18 – 30° . This makes predicting the correct $dp/d\Delta$ difficult, and there is range-varying waveform distortion associated with the triplicated arrivals [Walck, 1984], making back projection of the wavefield unstable. Back projection images for the European data contained significant image smearing, both spatially and temporally, relative to the images using North American data, mainly because the array footprint is smaller and the ruptures vary less in distance to the European stations. The European data are also at larger distances (~ 75 – 90°) where the incoming wavefield has a smaller $dp/d\Delta$, reducing space-time isolation of energy bursts, so we only present the results for North American stations.

[20] The back projections use n th root stacking, with some variation in image fidelity depending on the power (n) used. Areas from which the energy is radiated show up as “bright” spots in the grid for the time step at which that part of the fault was radiating P waves at periods of about 1 Hz. Finite array aperture produces time-varying streaking of the stacked images in the direction toward the array. Our source region grid is evenly spaced at 0.15° . The North American array results are shown in Figure 6. Figure 6 (top) show energy radiation at three time steps, one near the rupture initiation and two images from later parts of each rupture. For both events, the ruptures are dominated by a northeastward component of rupture, with distinct bursts of energy offset in space and time. The corresponding full time sequence of the back projections for each event are available as Animations S1 and S2 in the auxiliary material.¹ The approximate short-period time functions given by the peak amplitude of the image over the entire grid formed at each time step are shown for both events at the bottom of Figure 6. The limited network aperture smears the time resolution, and these radiation histories are only appropriate for the azimuth toward North America.

[21] In order to suppress the imaging artifacts intrinsic to this method, we deconvolve the back projection images by the corresponding space-time image formed for a smaller reference earthquake. As a reference event we chose the M_w 6.5 1 October 2006 preshock, which was large enough to

¹Auxiliary materials are available in the HTML. doi:10.1029/2008JB006280.

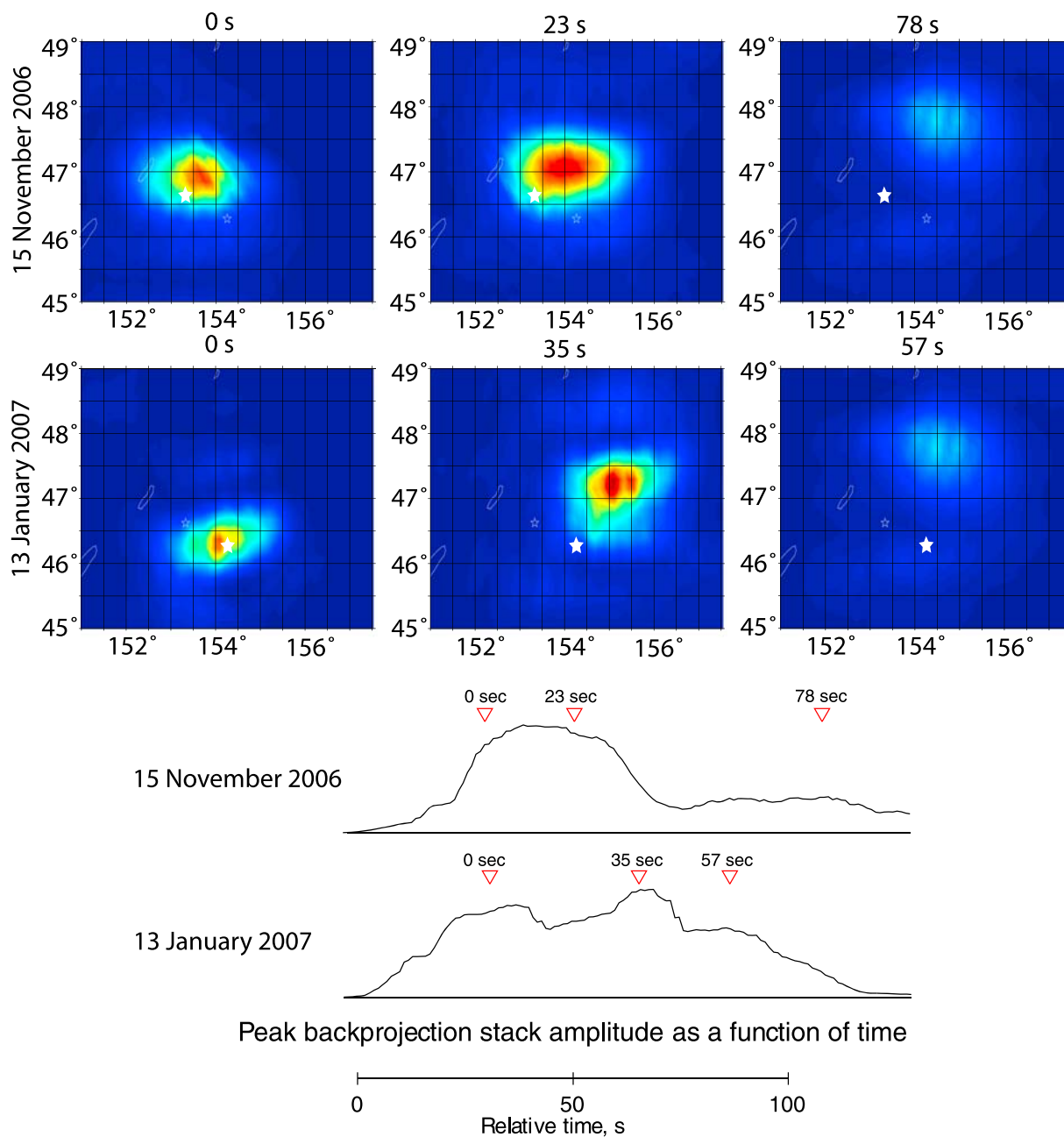


Figure 6. Images of the great doublet ruptures formed by short-period P wave back projection using signals from ~ 300 broadband seismic stations in western North America. (top) The 0.8–2.0 Hz vertical P wave energy stacked and integrated over 30 s time windows centered on three time points for the 15 November 2006 rupture, (middle) The same for the 13 January 2007 rupture. Warm colors identify regions of high short-period P wave energy radiation bursts relative to adjacent regions of low-amplitude or no P wave radiation (blue colors). The star in each image is the NEIC epicenter of the corresponding event. (bottom) The time varying peak amplitude of stacked signal over the back projection grid is shown for each event, with the time points corresponding to the images above indicated by the triangles. These peak amplitude traces are crude approximations of the short-period source time function corresponding to the direction to North America, but they are affected by the limited space-time isolation of radiation resulting from the finite array aperture.

generate high signal-to-noise ratio first arrivals. With a rupture length probably between 10 and 20 km, this event is small enough to approximate a point source for which the back projection smearing in space-time is primarily controlled by the array response, or point spread function [Xu et

al., 2009]. This event was used to remove the array response for both doublet events since the configurations are similar (Figure 7). In each case, only stations that recorded high signal-to-noise ratio ($> \sim 2$) P wave arrivals for both the reference and main event were used.

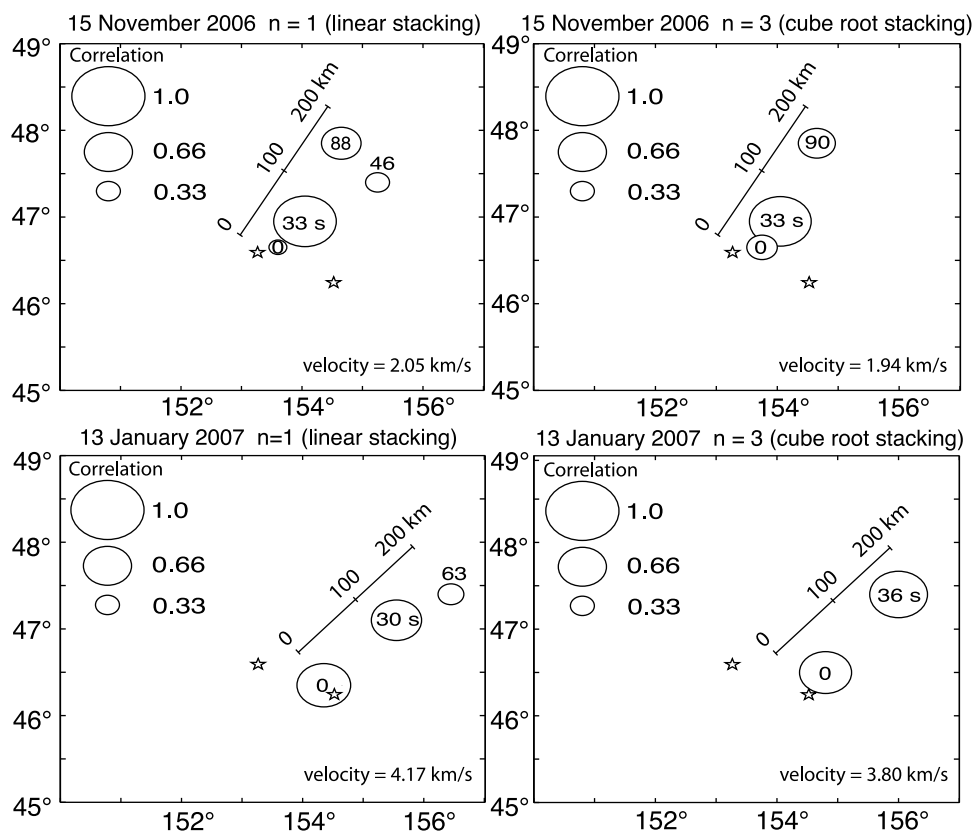


Figure 7. Short-period energy bursts and inferred rupture velocities for the Kuril doublet events on (top) 15 November 2006 and (bottom) 13 January 2007 determined by iterative deconvolution of the short-period back projection images by point spread functions determined for identical receiver configurations using the 01 October 2006 $M_w = 6.5$ preshock. The circle locations are at positions of maximum cross correlation coefficient (ccc) for each iteration, with the numbers indicating relative time. The circle diameters are scaled by the ccc and indicate relative amplitude of the subevents. The rupture velocities shown at the lower right of each plot are based on the two largest subevents, assuming continuous rupture propagation between them. (left) Back projection stack values are calculated using linear stacking and (right) the results based on values using cube root stacking. Linear stacking is more sensitive to individual seismogram amplitudes, while cube root stacking is almost entirely sensitive to the coherency of an arrival across the receiving array. The reference event used was close to the epicenter of the November event and had a similar focal mechanism to it.

[22] We approximate the three-dimensional (latitude, longitude and time) point spread function deconvolution by iteratively subtracting the reference event images for a large time window surrounding the event. We align the images using the space and time shifts that yield the maximum three-dimensional cross correlation coefficient between images for the reference event and main event. For each iteration, the values of the reference event subtracted are weighted by the reciprocal of the cross correlation coefficient, which effectively terminates the procedure when the maximum cross correlation coefficient becomes low. The result allows us to objectively identify the times and locations corresponding to regions of significant bursts of high frequency energy in continuous back projection images like Figure 6, which can then be treated as individual subevents. We obtain lower bounds of rupture length and duration using the subevents with the highest cross-correlation coefficients, of approximately 155 km and 88 s for the 15 November 2006 event and 130 km and 33 s for the 13 January 2007 event. If we infer smooth rupture

between the peak bursts for the two subevents with the highest cross correlation coefficients in the images, we obtain average rupture velocities of ~ 2.0 km/s for the 15 November 2006 event and ~ 4.0 km/s for the 13 January 2007 event. The values vary slightly depending on the power (n) used (Figure 7). The uncertainty in these rupture velocity estimates is $\sim 10\%$ based on the spatial distribution of the correlation coefficients for the major subevents.

[23] The imaging results identify components of north-eastward unilateral rupture along the trench strike for both events, and significant differences in the rupture velocity for the two events. For the 13 January 2007 event, finiteness along the trench favors either the CMT nodal plane steeply dipping toward the southeast, or the W phase nodal plane steeply dipping toward the northwest. This short-period rupture imaging is predominantly sensitive to local concentrations of high frequency radiation, and may not sense the smoother slip processes in the rupture. To explore directivity in the smoother rupture process, we must consider signals sensitive to the lower-frequency processes.

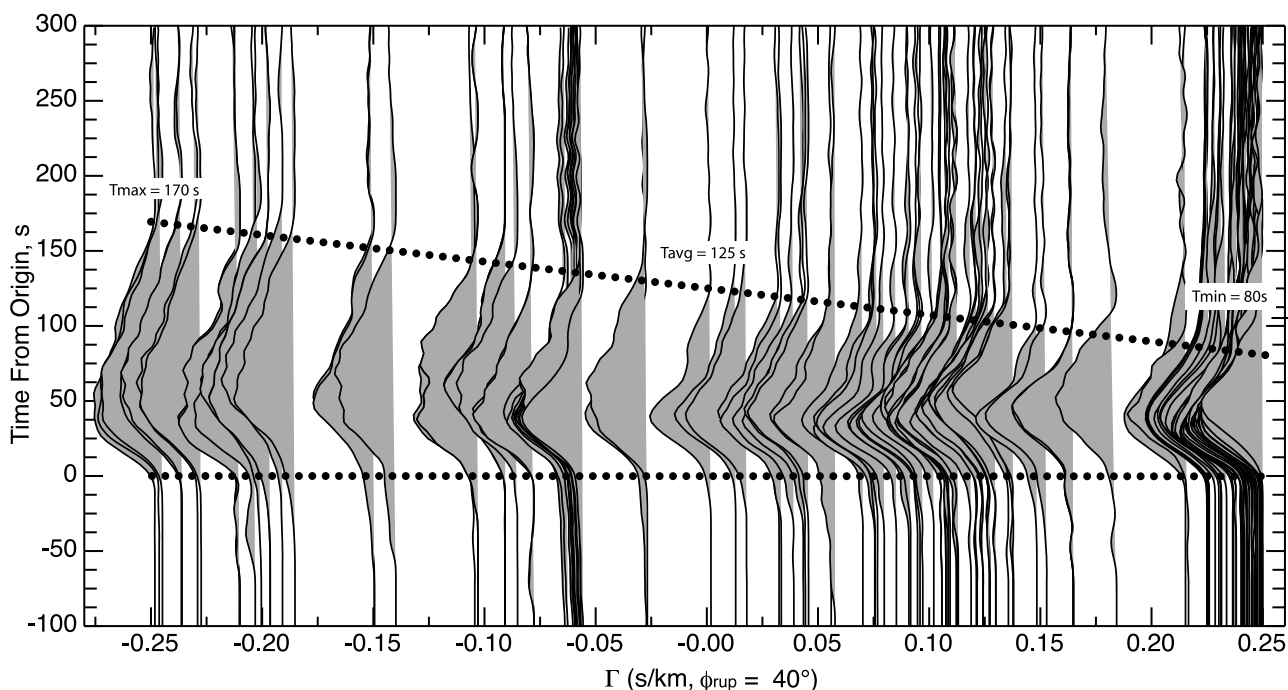


Figure 8. Rayleigh wave (R1) effective source time functions (STFs) plotted as a function of directivity parameter, $\Gamma = \cos(\phi_{\text{sta}} - \phi_{\text{rup}})/c$, where ϕ_{sta} is the station azimuth, ϕ_{rup} is an assumed unilateral rupture azimuth, and c is a reference phase velocity of 4.0 km/s, for the 15 November 2006 event, for an assumed rupture azimuth, ϕ_{rup} , of 40° . The phase of the STFs have been corrected for aspherical Earth structure, and minor additional adjustments were made on the initial alignments (horizontal dotted line). The minimum (T_{min}), average (T_{avg}), and maximum (T_{max}) durations are indicated, with the smooth move out being indicated by the slanted dotted line.

3.3. Surface Wave Source Time Function Directivity

[24] The Kuril Islands doublet events each provided hundreds of global broadband Rayleigh wave recordings. Since surface wave phase velocities are close to typical earthquake rupture speeds, the observed Rayleigh waveforms often contain large directivity effects [e.g., *Ammon et al.*, 2006a, 2006b, 2008]. Deconvolution of propagation operators can isolate the azimuthally dependent effective surface wave source time functions (STFs). The STFs can be used to constrain the rupture length, bound the rupture velocity, and image the smooth components of the seismic moment distribution. In previous analyses of large events we used signals from small earthquakes with similar location and fault orientation to a main shock as empirical Green's functions (EGFs) [e.g., *Ammon et al.*, 1993; *Velasco et al.*, 2000]. One limitation of EGFs is the difficulty of reliably isolating very long period (>250 s) components of the main shock due to the intrinsically weak long-period excitation for the smaller events. To circumvent this limitation *Ammon et al.* [2006a, 2006b] used point source synthetic seismograms (theoretical Green's functions: TGFs) computed using normal mode summation (periods > 20 s) for the PREM [*Dziewonski and Anderson*, 1981]. For large or slow ruptures the TGF analysis allows one to resolve directivity for periods long enough ($>\sim 100$ s) that a simple 1-D Earth model adequately accounts for excitation and propagation effects. For short overall rupture durations, the long-period restrictions of the TGF analysis blurs some important directivity patterns that are prominent at the

shorter periods, which were previously only resolved by using EGFs. The TGF deconvolution procedure was enhanced by applying path corrections for 3-D aspherical structure for the Rayleigh waves using a degree 36 phase velocity model from *Boschi and Ekström* [2002]. This achieved better phase alignment and coherent STFs for periods down to ~ 30 s, comparable to the periods typically resolved using EGFs. To further improve the STF alignment, we picked the onset time of each STF by fitting a line to the initial increase in moment rate and used the line's intercept as the rupture onset.

[25] The aligned STFs for the 2006 event are shown in Figure 8, arranged by directivity parameter, $\Gamma = \cos(\phi_{\text{sta}} - \phi_{\text{rup}})/c$, where ϕ_{sta} is the station azimuth, ϕ_{rup} is an assumed unilateral rupture azimuth, and c is a reference phase velocity (c is chosen as 4.0 km/s, the phase velocity for 80 s period Rayleigh waves for model PREM). STFs will be narrower and larger amplitude for positive values of Γ , as wave energy piles up for signals propagating in the direction of rupture, while STFs will be broader and lower amplitude for negative values of Γ . We assume a rupture azimuth $\phi_r = N40^\circ E$, corresponding to rupture along the strike of the subduction zone. The dramatic broadening of the source functions for negative directivity parameters relative to the narrower source functions for positive directivity parameters indicate predominantly unilateral rupture toward the northeast for this event. Assuming a simple unilateral rupture, the linear increase in duration from $T_{\text{min}} \sim 80$ s to $T_{\text{max}} \sim 170$ s as a function of directivity parameter, Γ , is consistent with a total duration of $T_{\text{avg}} \sim 125$ s and a fault length of $L = c/2 \times$

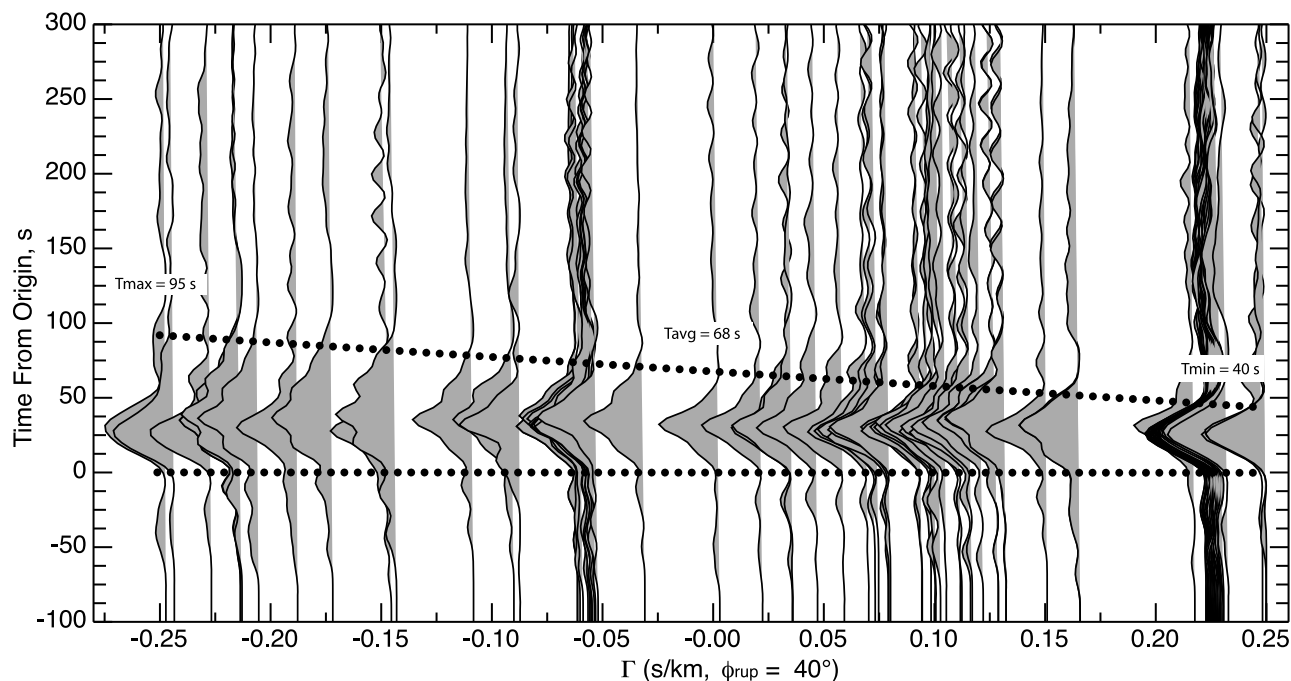


Figure 9. Rayleigh wave (R1) effective source time functions (STFs) plotted as a function of directivity parameter, $\Gamma = \cos(\phi_{\text{sta}} - \phi_{\text{rup}})/c$, where ϕ_{sta} is the station azimuth, ϕ_{rup} is an assumed unilateral rupture azimuth, and c is a reference phase velocity of 4.0 km/s, for the event of 13 January 2007, for an assumed rupture azimuth, ϕ_{rup} , of 40° . The phase of the STFs have been corrected for aspherical Earth structure, and minor additional adjustments were made on the initial alignments (horizontal dotted line). The minimum (Tmin), average (Tavg), and maximum (Tmax) durations are indicated, with the smooth move out being indicated by the slanted dotted line.

($T_{\text{max}} - T_{\text{min}}$) = 180 km, for $c = 4$ km/s. Assuming a risetime of $0.2 \times T_{\text{avg}}$, these values give an estimated rupture speed of ~ 1.8 km/s. The uncertainty in the rupture speed estimate depends on the measured durations and the assumed risetime, and we estimate it by computing results for 100,000 cases where we assign random perturbations (up to ± 10 – 15 s uncertainties) to T_{max} and T_{avg} durations and to the risetime. The 80% confidence range obtained for the rupture velocity is 1.7 ± 0.3 km/s. The 80% confidence range on fault length is 175 ± 25 km, roughly consistent with the aftershock extent to the northeast of the hypocenter, which is about 200 km (Figure 3). A comparable rupture velocity estimate of 1.8 km/s was obtained by *Baba et al.* [2009] using analysis of seismic and tsunami data.

[26] A similar analysis for the 13 January 2007 event (Figure 9) indicates a weaker component of northeast directivity. Assuming a simple unilateral rupture, the linear increase in duration from $T_{\text{min}} \sim 40$ s to $T_{\text{max}} \sim 95$ s as a function of directivity parameter, Γ , is consistent with a total duration of $T_{\text{avg}} \sim 68$ s and a fault length of $L = c/2 \times (T_{\text{max}} - T_{\text{min}}) = 110$ km, for $c = 4$ km/s. For a risetime of $0.2 \times T_{\text{avg}}$, we get an estimated rupture velocity of 2.0 km/s. However, the estimated fault length is substantially shorter than the aftershock zone, suggesting that the assumption of unilateral rupture is not justified in this case. Assuming an asymmetric bilateral rupture, we can use the average duration of the azimuthally varying portion of the STFs (28 s) and the associated resolved unilateral component of rupture length of 110 km, to find an upper bound on the rupture

velocity of 4.0 km/s. Alternatively, using the ~ 180 km extent of early aftershocks to the northeast of the hypocenter for the overall length, the average STF duration of 68 s, and accounting for the risetime, provides an estimated rupture velocity of ~ 3.3 km/s. The latter two estimates are compatible with the short-period body wave estimate, and the asymmetric bilateral nature of the rupture is confirmed by the finite source inversions below. Again using 100,000 simulations with uncertainties assigned to the T_{min} , T_{max} and risetimes, yields 80% confidence ranges of 2.6 ± 1.0 km/s for rupture velocity, and 100 ± 40 km for fault length. The large uncertainty on rupture velocity reflects the possibility of asymmetric bilateral rupture. In the finite fault inversions below we present results for rupture speeds of 1.8 km/s and 3.5 km/s for the 15 November and the 13 January events, respectively, although we explored a broad range of rupture velocities spanning all of the estimates for each event.

4. Finite Fault Rupture Images of the Great Events

[27] Guided by the constraints on overall faulting geometry and rupture velocity from the preceding analyses, we developed finite fault slip models for the two great events. We initially inverted large P and SH data sets for each event using very flexible finite source algorithms that allow for changes in subevent moment tensor with unconstrained or constrained rupture velocities for variable hypocentral depths and fault dimensions [*Kikuchi and Kanamori,*

1991]. This suite of inversions convinced us that the body waves provide no clear indication (or resolution) of change in fault orientation during rupture for either event, and that the point source solutions discussed above all provide adequate basic geometries for matching the teleseismic waveforms for both events.

[28] The inversions for our final slip models prescribe the fault geometries, subdivide the rupture area into a grid of subfaults, and specify the rupture velocity. The rupture area expands with a constant rupture velocity from the hypocenter and we allow distinct source time functions for each subfault element, with a linear inversion of teleseismic P wave and, in some cases, SH wave observations. The rake is allowed to vary at each subfault. Green functions were computed for simple layered source and receiver structures connected by geometric spreading for a deeper Jeffreys-Bullen Earth model. The inversions assume frequency-independent attenuation models with $t^* = 1$ s for P waves and $t^* = 4$ s for S waves (t^* is the path integral of the ratio of travel time to attenuation quality factor for each wave type), and determine subevent point source seismic moment, which we convert to slip using the grid spacing dimensions and the local shear modulus inferred from the source velocity structure.

4.1. Body Wave Selection and Processing

[29] We used body waves from distant stations to minimize PP and SS interference. We performed inversions of data with and without deconvolution of the individual instrument responses. Instrument deconvolution tends to enhance long-period noise, causing baseline uncertainties, particularly for a long duration rupture like that for the 15 November 2006 event. Our final inversions are performed for band-pass-filtered deconvolutions with a passband of 1–200 s, which is also applied to our Green functions. We do not account for core reflections, which are generally of small amplitudes; where possible we checked this by examining the waveforms from smaller events in the sequence. We selected subsets of the huge available global data set to balance azimuthal weighting in the inversions.

[30] Relative timing is of great importance for finite source inversions using body waves, because small differential times within the waveforms provide the spatial resolution. Both great earthquakes have somewhat emergent initial P wave and SH wave onsets, thus travel time alignment is not trivial. In order to reduce the subjectivity of onset picks, we used the NEIC hypocentral locations and computed travel times for the PREM Earth model, applying aspherical path corrections for a P wave tomographic model [Houser *et al.*, 2008] and an SH wave tomographic model [Mégnin and Romanowicz, 2000]. This gave relative alignments very consistent with direct picks of the more impulsive arrivals. SH waves were used for azimuths away from clear nodes. Slight adjustments in SH wave onset times for a few stations were made after initial inversions established that the entire waveform was slightly shifted.

4.2. The 15 November 2006 Fault Rupture

[31] For the finite source inversions of the 15 November 2006 event, we search for optimal fault plane geometry in the vicinity of the W phase and CMT best double couple orientations (Table 1). Based on variance reduction of finite

fault inversions, our final fault geometry has $\phi = 220^\circ$, $\delta = 15^\circ$, and for fixed rake inversion, $\lambda = 103^\circ$. This shallow dipping plane has a strike along the trench axis; strike and average rake trade off to some degree in the finite fault solutions. Dip is not well resolved and trades off directly with M_0 , so we constrain the dip based on aftershock depth modeling.

[32] A large, well-distributed set of P waves was inverted with the variable rake algorithm. Figure 10a shows the slip model and source time function, and Figure 10b shows the waveform matches obtained for a rupture velocity of 1.8 km/s, as indicated by the directivity analyses. The source velocity structure included a 3 km deep ocean layer overlying a 15 km thick crust with $V_p = 6.5$ km/s, $V_s = 3.74$ km/s and $\rho = 2.87$ g/cm³, and a mantle layer with $V_p = 7.8$ km/s, $V_s = 4.4$ km/s and $\rho = 3.3$ g/cm³. The hypocentral depth was set to 15 km (12 km deep into the crust), based on the modeling of nearby aftershocks. The subfault grid had 20 km spacing along strike and 10 km spacing along the dip direction. Each subfault source time function was parameterized by 6 overlapping 4 s duration triangles offset by 2 s each, giving subfault rupture durations of 14 s. The slip is found to be concentrated in the upper portion of the rupture plane. The slip extends along strike about 240 km and along dip about 100 km, with only modest variations in the rake over the fault plane. The average rake is 96° , slightly higher than the CMT solution due primarily to the 5° rotation of the strike. The source time function has a total duration of about 115 s, with three concentrations of slip and a total seismic moment of 5.0×10^{21} N m ($M_w = 8.4$). The primarily unilateral rupture extends toward the northeast, consistent with the overall R1 STF directivity in Figure 8. Comparison with the positions of the high frequency bursts of energy imaged by the short-period back projection (Figure 7) suggests that the large secondary bursts are associated with the two northeastern patches of enhanced slip. The patch of slip near the hypocenter appears to have failed bilaterally, and did not radiate a strong initial high frequency P wave toward the North American azimuth. But as the rupture propagated northeastward two regions produced enhanced bursts of short-period radiation toward North America, perhaps influenced by directivity. The average slip over the entire fault plane for this model is ~ 4.6 m, but averages ~ 6.5 m over all well-resolved subfaults having peak moment greater than 30% of the maximum subfault moment (these are concentrated in the depth range 3 to 20 km). Inversions for varying rupture velocities and varying fault dimensions recover similar basic features, especially for the moment rate function, and yield comparable variance reductions, but with direct trade offs between rupture velocity and spatial location of slip. Assuming a deeper hypocenter shifts slip to greater depth for the first subevent, but the models clearly favor primarily shallow slip to match the P waves.

[33] While the various finite slip models noted in Table 1 differ in detail, they all have northeastward directivity with slip tending to be concentrated at relatively shallow depths. Our overall results are similar to those of Ammon *et al.* [2008], but we note one important difference. The models presented here have more slip at shallower depths, and less slip at greater depths. Ammon *et al.* [2008] noted a lack of resolution of the deeper slip. One factor affecting the

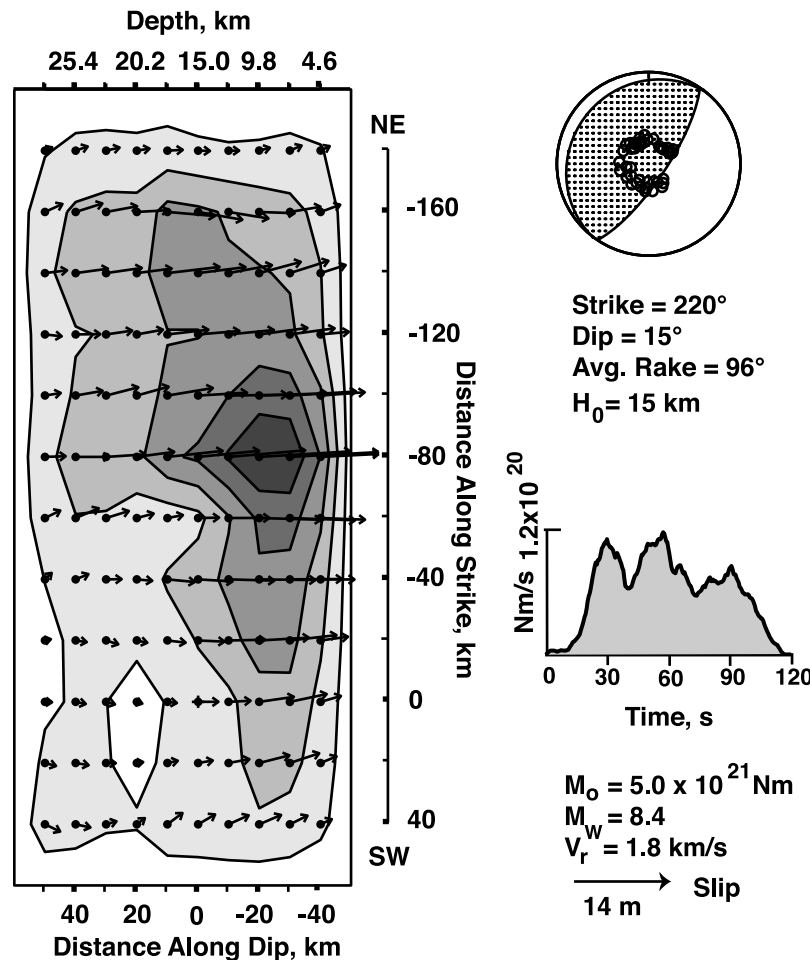


Figure 10a. Finite source model for the 15 November 2006 event from inversion of teleseismic P waves. The fault plane orientation (top right) is for the northwest dipping plane from a search over varying strike and has a strike of 220° and a dip of 15° . The hypocentral depth was set to 15 km, slip on a 12×10 grid with 20 km spacing along strike and 10 km spacing downdip was determined assuming a rupture velocity of $V_r = 1.8$ km/s. The rake for each subfault was allowed to vary, and the slip magnitudes and directions are indicated on the left. The source time function is shown on the right, and the seismic moment estimate of 5.0×10^{21} N m gives an M_w of 8.4. The slip contours are for 1, 4, 7, 10, and 13 m as the gray tone darkens.

shallow slip to the northeast is the 10° change in strike geometry. *Ammon et al.* [2008] adopted the CMT strike, which is slightly oblique to the trench geometry. Here, we adopt the trench geometry, which increases the area available for shallow slip in the northeast. Our moment is about 9% larger than found by *Ammon et al.* [2008], and appears too large by 50% or more relative to determinations from surface waves and the W phase (Table 1) (allowing for variations in moment caused by differences in dip estimate). If we use a 10° dip, we get a slightly smaller moment of 4.7×10^{28} N m, with almost the same slip distribution, and this shallower dip would increase some of the long period moment estimates to compatible levels. Stable resolution of the baseline for the P waves is an issue for all body wave inversions, and we view the primary contribution of our finite source models as being resolution of the spatial pattern and depth distribution of the slip, with the magnitude of slip likely being somewhat overestimated.

4.3. The 13 January 2007 Fault Rupture

[34] The mechanism for this event is surprisingly uncertain, with significant differences between the W phase, CMT and other solutions. As noted above, aftershock relocations do not appear to unambiguously resolve the fault plane, and the short-period and STF directivity favor rupture along the trench strike and trend of the aftershocks, which tends to favor one plane in each point source solution. Finite source models for the 13 January 2007 event were obtained for the W phase, CMT, Polet and many other fault geometries (Table 2) dipping either southeast or northwest in an effort to resolve the fault plane ambiguity. Basically similar slip distributions and overall waveform fits are found for all of the fault orientations and model parameterizations that we considered, with concentration of slip in the upper 25 km of the oceanic lithosphere, and little independent constraint on rupture velocity or precise geometry. For lower rupture velocities near 2 km/s the estimated average slip at crustal

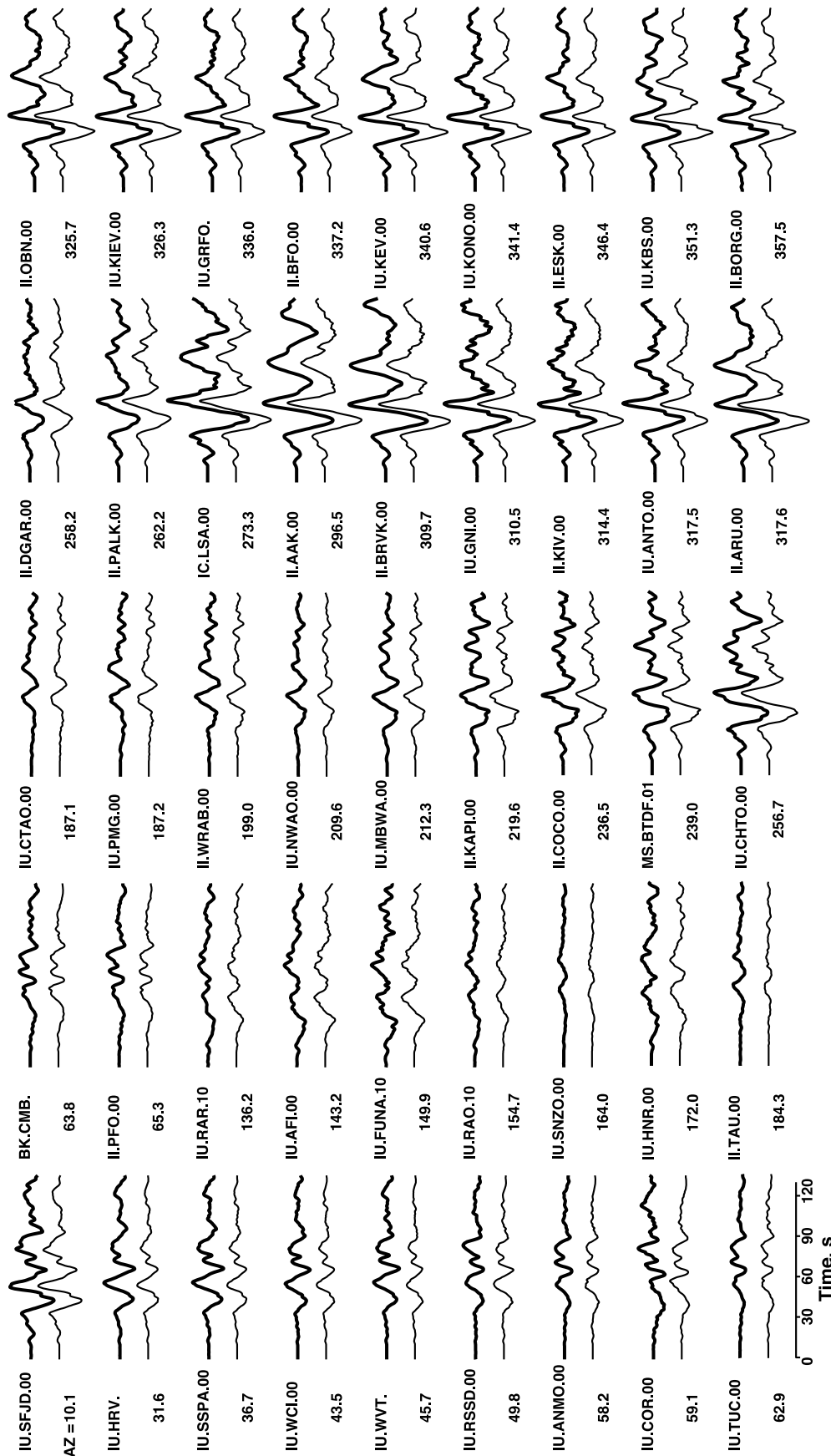


Figure 10b. P wave waveform fits for the inversion for 15 November 2006, corresponding to Figure 10a. Data for each station are indicated by the heavy lines and synthetics by the light lines. The azimuth of each station is indicated.

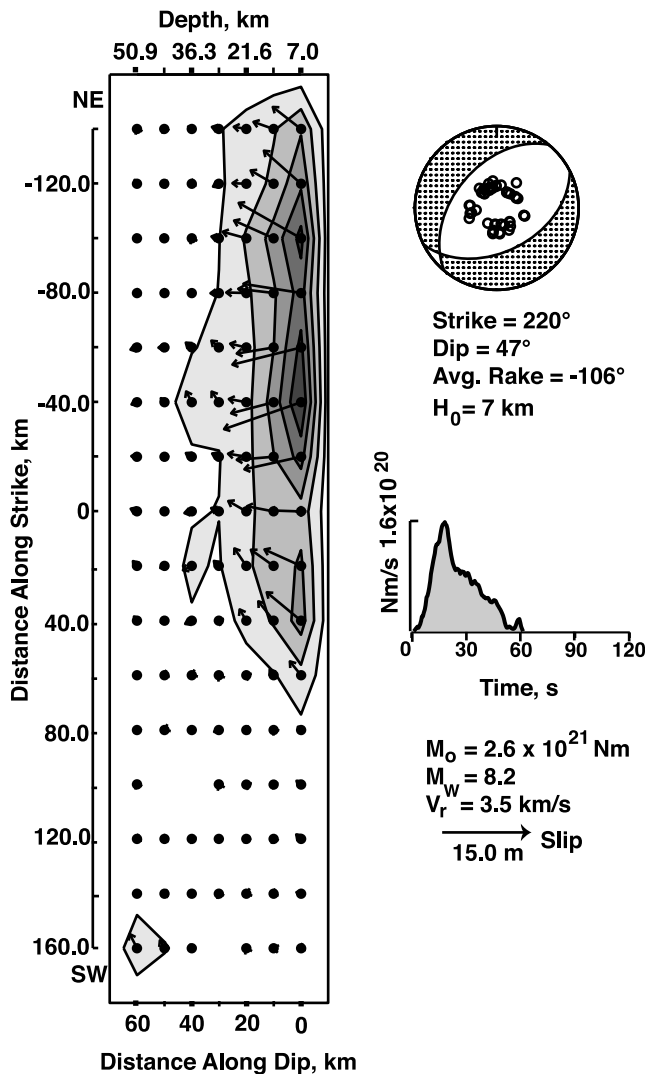


Figure 11a. Finite source model for the 13 January 2007 event from inversion of teleseismic P and SH waves. The fault orientation is the northwest dipping plane of a modified version of the W phase solution, with $\phi = 220^\circ$ and $\delta = 47^\circ$ (top right). The hypocentral depth was set to 7 km, slip on a 16×7 km grid with 20 km spacing along strike and 10 km spacing downdip was determined assuming a rupture velocity of $V_r = 3.5$ km/s. The rake for each subfault was allowed to vary, and the slip magnitudes and directions are indicated on the left. The source time function is shown on the right, and the seismic moment estimate of 2.6×10^{21} N m gives an M_w of 8.2. The slip contours are for 1, 4, 7, 10, and 13 m as the gray tone darkens.

depths is very large, over fault lengths of 90–110 km. Larger rupture velocities of up to 3.8 km/s (the crustal shear velocity) yield proportionally lower average slip and longer increased rupture lengths of 220–260 km. Higher rupture velocities are compatible with the estimates of ~ 4.0 km/s from the short-period back projection (Figure 7) and 3.3 to 4.0 km/s from the R1 STF analysis. The fit to P waveforms at stations to the south tends to be better for finite source models using the northwest dipping plane, but stations to

the east are fit slightly better for the finite source models using the southeast dipping geometry.

[35] Figure 11a shows the slip distribution obtained from fitting P and SH waves with the variable rake algorithm using the northwest dipping fault for a mechanism modified from the W phase solution by grid searching over many orientations and seeking the best variance reduction for a specified rupture velocity of 3.5 km/s. This mechanism has a fault plane with orientation $\phi = 220^\circ$ and $\delta = 47.0^\circ$. This is rotated by -11° in strike and -24° in dip relative to the W phase solution, and the shallower dip improves the overall fit compared to the W phase solution. The source velocity model in this case had a 4 km deep ocean over a 6 km thick crust with $V_p = 6.8$ km/s, $V_s = 3.8$ km/s and $\rho = 2.7$ g/cm³, and a mantle with $V_p = 7.8$ km/s, $V_s = 4.4$ km/s and $\rho = 3.5$ g/cm³. The subfault grid spacing was 20 km along strike and 10 km along the dip direction. The subfault source time functions were parameterized by 6 overlapping 4 s duration triangles shifted by 2 s each, giving subfault rupture durations of 14 s. The rake is found to be only modestly variable, with an average value of -106° . For this case, using a hypocentral depth of 7 km gives a better solution than a deeper hypocenter as it allows minor northwestward propagation of the rupture. The moment rate function has one main pulse with a broadened shoulder that is enhanced by inclusion of the SH waves, giving a northeastward extension of the slip. The two primary high frequency bursts in the short-period back projection image in Figure 7 are separated by about the length of the strong slip patch in the finite fault model. The slip is largest within the crustal layer, with significant slip being confined within a rupture area of 220×30 km. The average slip for subfaults with moment greater than 30% of the peak subfault moment is 6.7 m, over a region of 5,600 km². The total seismic moment estimate is 2.6×10^{21} N m ($M_w = 8.2$). The rupture has a duration of at least 60 s, and the early portions of the waveforms are quite well fit (Figure 11b), but there does appear to be coherent energy later in the body waves. For a high rupture velocity, simply extending the fault dimensions leads to late, spatially poorly resolved slip far along strike to the northeast, beyond the aftershock zone. Keeping the fault dimensions and rupture velocity fixed, but allowing for 15 triangular subevents on each subfault (total subfault rupture durations of 32 s) provides about 30% improvement in variance reduction and total rupture duration of about 90 s, with smooth slip having the same basic pattern as in Figure 11b and 50% increase in seismic moment. In all inversions that we ran, over 82% of the seismic moment is released above 33 km depth, and we cannot robustly resolve the presence of any deeper slip. If we constrain the fault model to extend no deeper than 33 km, the residual variance in the solution is only 2% higher than for the model in Figure 11a, so deeper slip is not required by the data. The overall waveform fit is not a good as might be hoped, suggesting that a uniform rupture velocity with a narrow rupture annulus and a constant fault geometry may not be optimal for this rupture, and indeed inversions that do not prescribe a rupture velocity at all find better fits to the data with some later, somewhat deeper slip on the fault. This complexity may be associated with the mechanism variability found for different data sets, but we cannot

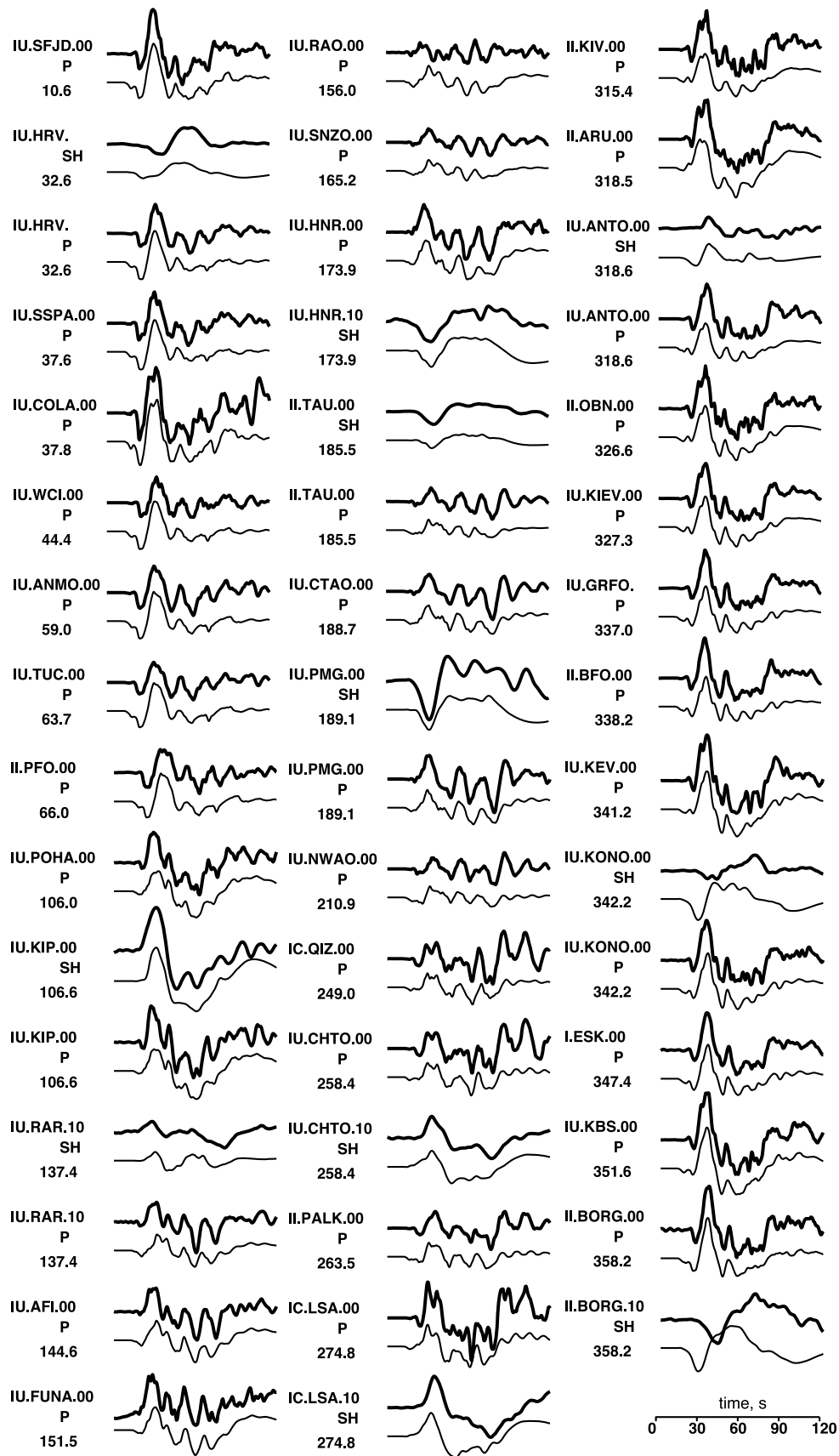


Figure 11b. *P* and *SH* wave waveform fits for inversion for 13 January 2007 for the northwest dipping fault plane solution shown in Figure 11a. Data for each station are indicated by the heavy lines and synthetics by the light lines. The azimuth of each station is indicated.

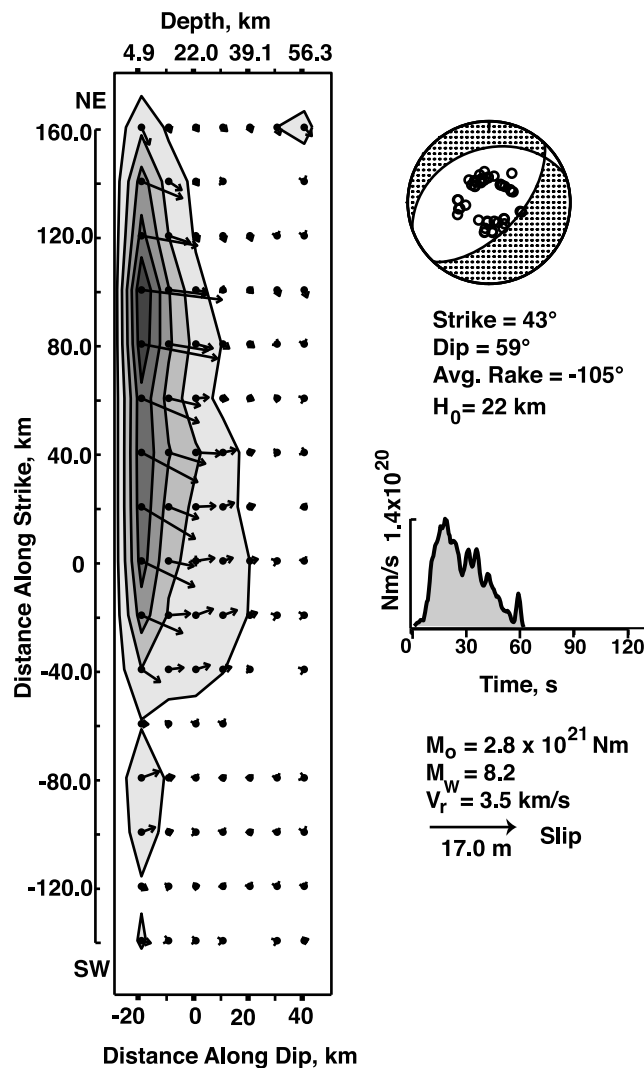


Figure 11c. Finite source model for the 13 January 2007 event from inversion of teleseismic P and SH waves. The fault orientation is the southeast dipping plane of the CMT solution, with $\phi = 43^\circ$ and $\delta = 59^\circ$ (top right). The hypocentral depth was set to 22 km, slip on a 16×7 km grid with 20 km spacing along strike and 10 km spacing downdip was determined assuming a rupture velocity of $V_r = 3.5$ km/s. The rake for each subfault was allowed to vary, and the slip magnitudes and directions are indicated on the left. The source time function is shown on the right, and the seismic moment estimate of 2.8×10^{21} N m gives an M_w of 8.2. The slip contours are for 1, 4, 7, 10, and 13 m as the gray tone darkens.

resolve the details and view the model in Figure 11a as a first-order solution only.

[36] Figure 11c shows the slip distribution for the same data set, velocity model, rupture velocity, subfault dimensions and algorithm as in Figure 11a, but using the southeast dipping fault in the CMT solution, which is the same orientation used by *Ammon et al.* [2008]. The rake is again found to be fairly stable, with an average value of -105° compared to -115° in the CMT solution. For this case, having the hypocenter at a depth of about 22 km gives a

better solution than a shallower hypocenter as it again allows minor northwestward propagation of the rupture. The moment rate function and northeastward distribution of slip are very similar to the solution in Figure 11a. The slip is largest within the crustal layer, with average slip of about 7.7 m over the 5200 km² of the fault plane where subfault moment is greater than 30% of the peak subfault moment. The overall seismic moment estimate is 2.8×10^{21} N m ($M_w = 8.2$). The waveform fit (Figure 11d) is comparable to the solution for the northwest dipping geometry, with both models giving about 72% variance reductions. Allowing for longer (32 s) subfault rupture durations for this geometry improves the variance reduction to 83%, but involves a 56% increase in seismic moment and almost the same spatial distribution of slip. The only significant difference in waveform fit between the northwest dipping and southeast dipping solutions is for the waveform alignment for SH data to the northeast (stations HRV and BORG), where the CMT solution fits the arrival times better. Unfortunately, the aspherical model corrections for these two stations vary significantly between tomographic models, and use of another model such as *Grand* [2002] gives better alignment for these two stations for the northwest dipping fault model. Overall, we have not found a compelling line of evidence from the finite source inversions to clearly favor one fault orientation over the other. This is largely due to the shallow depth and intermediate dip of the rupture. Other finite source models noted in Table 2 tend to share similar slip concentrations at shallow depth, with varying degrees of rupture asymmetry relative to our models. Our seismic moment estimates are again $\sim 50\%$ higher than long-period determinations, so we view our absolute slip values as likely being overestimated.

4.4. Source Spectra for the Doublet

[37] The dramatically different moment rate functions and source spectra for the two great events are compared in Figure 12. The body wave spectral amplitudes for the 13 January 2007 event are significantly larger, by ratios of 4 to 7, than those for the 15 November 2006 event, despite the larger seismic moment of the earlier event (we use CMT estimates of the seismic moment for this plot). The January event thus has larger 1 s period body wave magnitude (m_b) and 20 s period surface wave magnitude (M_s) than the November event. This short-period enrichment is similar to that for the 1933 Sanriku earthquake [*Kanamori*, 1971], and may reflect rupture on a fault with little cumulative slip and correspondingly less fault gouge and fault zone broadening. Seismic energy release for the November event (9.6×10^{15} J) is less than for the January event (4.3×10^{16} J), and the energy/moment ratios are 2.7×10^{-6} and 2.4×10^{-5} , respectively. The factor of 9 contrast in scaled energy indicates significant differences between the interplate and intraplate faulting environments, as does the greater rupture velocity preferred for the intraplate faulting. Triggering of a large order rise rupture with strong high frequency shaking constitutes an important potential seismic hazard that needs to be considered in other regions.

4.5. The 15 January 2009 Fault Rupture

[38] The large compressional trench slope event of 15 January 2009 is of particular interest because it is located

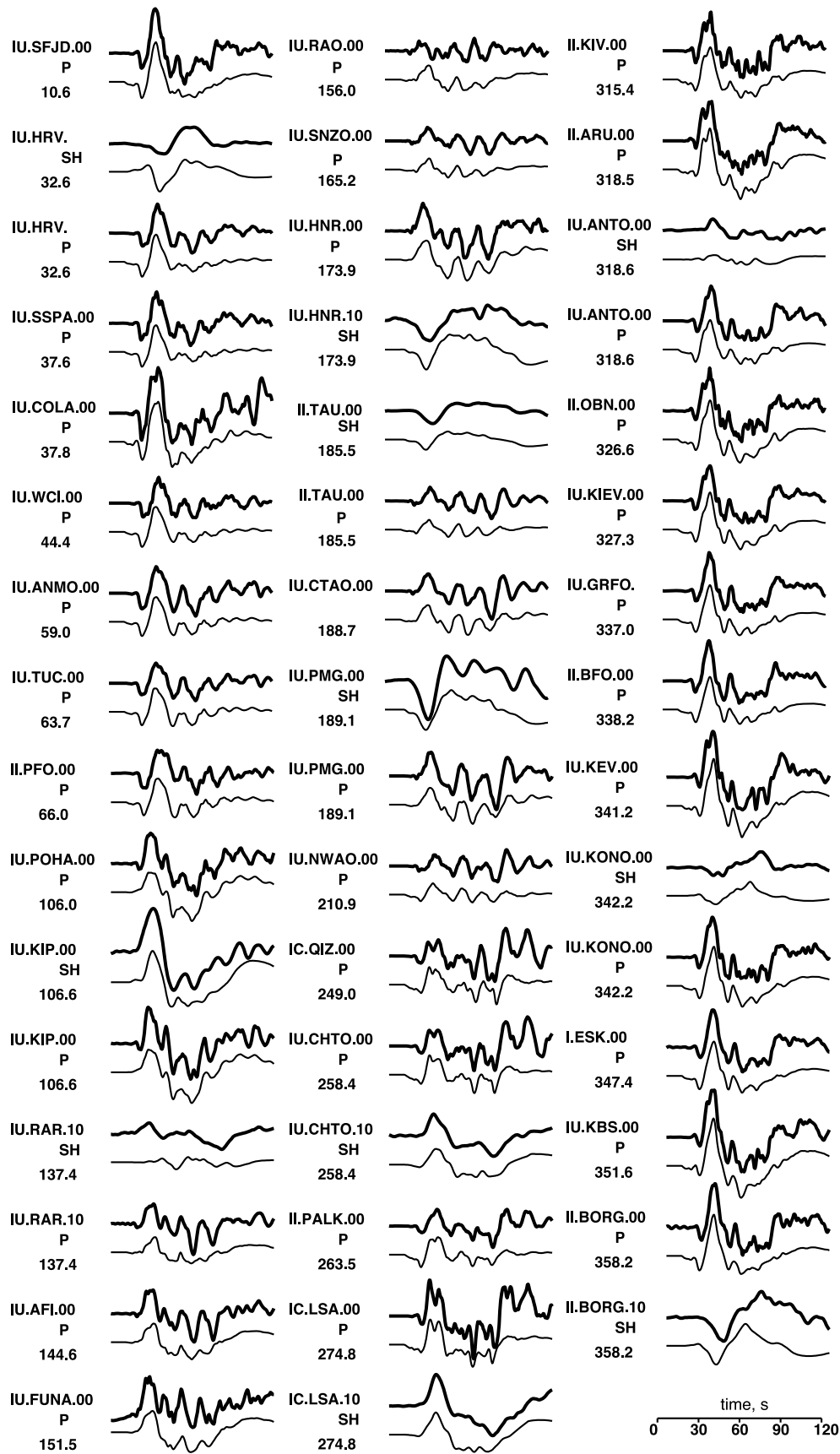


Figure 11d. *P* and *SH* wave inversion waveform fits for 13 January 2007 for the southeast dipping plane in the CMT solution shown in Figure 11c. Data for each station are indicated by the heavy lines and synthetics by the light lines. The azimuth of each station is indicated.

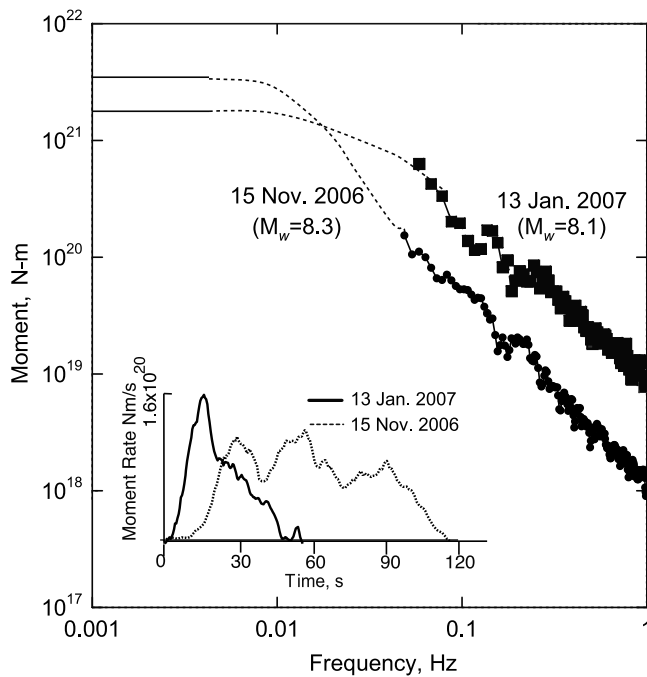


Figure 12. Moment rate spectra for the 15 November 2006 and 13 January 2007 events based on teleseismic seismic moment estimates and P wave spectra. Note the larger high frequency amplitudes for the smaller seismic moment 2007 event. This is associated with higher energy release and higher energy/seismic moment ratio for the January event. The inset compares the source time functions for the doublet events from the body wave finite source inversions. Note the differences in peak moment rate, total duration, and overall complexity.

in the vicinity of the extensional sequence. A large data set of 55 P waves was inverted for the source process of this event; the results are summarized in Figure 13. A relatively simple, concentrated slip model is resolved, with a centroid depth of 44.6 km and an $M_w = 7.4$, both consistent with the CMT solution. The slip appears to extend over a rupture area of about $35 \times 50 = 1750 \text{ km}^2$, spanning a depth range of 35–55 km or so, but this finite extent is not well resolved due to lack of directivity in the rupture process. The depth range is significantly deeper than that for the primary slip in the 13 January 2007 rupture.

[39] The 2009 compressional event epicenter is located very close to that of the 1963 compressional event (Figure 14). By filtering the broadband P wave signals for the 2009 event to have World Wide Standardized Seismograph Network (WWSSN) Sprengnether 30–100 instrument responses, we could directly compare data for the 1963 and 2009 events using the digitized WWSSN signals for the 1963 event from *Raeesi and Atakan* [2009]. Only a few stations remain collocated, but several others are in close proximity, and we find basically similar waveforms, but the 2009 event produced P wave signals on average 1.8 times stronger than the 1963 event. This is consistent with the difference in M_S values (7.5 versus 7.2 for 2009 and 1963, respectively). *Raeesi and Atakan* [2009] tabulate centroid depth estimates for the 1963 event ranging from 26 to 50 km, and the finite source model presented in their paper

indicates to us a slightly shallower depth range (~ 25 – 36 km) for the well-resolved slip in the 1963 event compared to our result of 35–55 km for the 2009 event, although their estimated moment for the 1963 event is much larger than suggested by our P waveform amplitude comparisons. Their relocated hypocentral depth estimate for the 1963 event is 29.5 km. The depth estimate of 0–50 km for the 1963 event given by *Christensen and Ruff* [1988] is hard to evaluate, since it is based on several single-station deconvolutions, and their method mainly bounds the maximum viable point source depth. *Seno and Yamanaka* [1996] report a depth of 32–52 km for the 1963 event, similar to our estimate for the 2009 event. We infer that both compressional events have their primary slip at greater depths than the 2007 extensional event.

5. Discussion

[40] The seismic models obtained in this study are generally compatible with models obtained for tsunami records from tide gauges and Deep-ocean Assessment and Reporting of Tsunamis (DART) buoys, which are summarized in Tables 3 and 4. Tsunami modeling is particularly sensitive to initial sea surface displacement, which is in turn controlled by ocean bottom displacement (basically proportional to the product of fault area and slip). Assuming a reasonable average rigidity allows computation of seismic moment from the tsunami-based dislocation models, which is perhaps the best measure to compare with the seismic results in Tables 1 and 2. A slightly higher rigidity is used for the 2007 event, given that it ruptured into the deep crust and upper mantle of the oceanic lithosphere. *Rabinovich et al.* [2008] constrained their solutions to match the seismic moment estimates from C. Ji (Rupture process of the 2006 NOV 15 magnitude 8.3 - KURIL Island earthquake (revised), 2006, available at http://earthquake.usgs.gov/eqcenter/eqinthenews/2006/usvcam/finite_fault.php; Rupture process of the 2007 Jan 13 magnitude 8.1 - KURIL Island earthquake (revised), 2007, http://earthquake.usgs.gov/eqcenter/eqinthenews/2007/us2007xmae/finite_fault.php). *Rabinovich et al.* [2008] also made a theoretical correction of a factor of 2.6 in scaling calculated ocean bottom displacement to water surface displacement, to account for the large water depth in the trench above the 2007 rupture zone. *Tanioka et al.* [2008] made a different correction for large water depth. Table 4 contains a list of seismic moment estimates from the tsunami modeling, along with estimates for a uniform value of rigidity and with correction for the water depth effect. Tsunami-based estimates of seismic moment for the 2006 event of 2.0 – $3.1 \times 10^{21} \text{ N m}$ overlap the range of estimates from seismic methods, as do the values of 1.3 – $2.9 \times 10^{21} \text{ N m}$ for the 2007 event. While the seismic finite fault slip models have localized regions of high slip, it is average slip values that control tsunami excitation, so we can infer that our seismic faulting models have general compatibility with the tsunami observations, within respective uncertainties.

[41] *Song and Simons* [2003] examined gravity variations along many of the world's subduction zones and suggested that large underthrusting events correlate with negative trench-parallel gravity anomalies (TPGA). However, the 15 November 2006 Kuril underthrusting event ruptured a

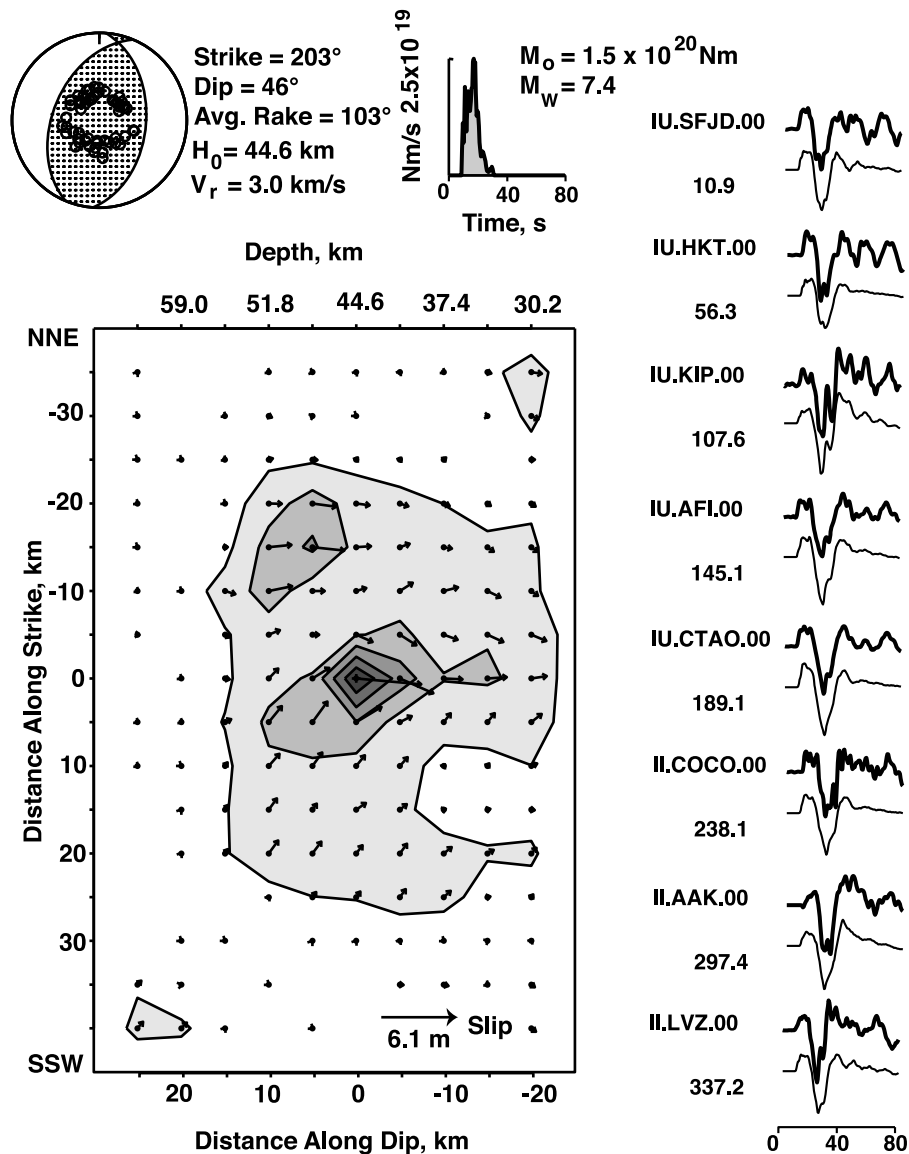


Figure 13. Finite source model for the 15 January 2009 event from inversion of teleseismic P waves. The fault orientation is the northwest dipping plane of the CMT solution, with $\phi = 203^\circ$ and $\delta = 46^\circ$ (top left). The hypocentral depth was set to 44.6 km, slip on a 16×10 km grid with 5 km spacing along strike and downdip was determined assuming a rupture velocity of $V_r = 3.0$ km/s. The rake for each subfault was allowed to vary, and the slip magnitudes and directions are indicated on the left. The source time function is shown at the top, and the seismic moment estimate of 1.5×10^{20} N m gives an M_w of 7.4. Representative P wave observations (bold lines) and synthetics (light lines) are shown at various azimuths. The entire inverted data set involved 55 observations with the coverage indicated in the focal mechanism at the top left. The slip contours are for 0.5, 1.5, 2.5, 3.5, and 4.5 m as the gray tone darkens.

region with a relatively strong positive TPGA over most of the interplate fault, at odds with the typical pattern. Our slip model has slip concentrated at shallower depths than found for other great interplate regions along the arc, so the relation to TPGA may be somewhat distinct. *Llenos and McGuire* [2007] found that the 2006 event was also distinctive from several other large events in having a rupture that terminated in a region lacking any lateral increase in TPGA. Still, the 2006 rupture is located beneath the only region of the Kuril Islands arc with a well

developed fore-arc basin. Large seismic slip has been noted to occur elsewhere below fore-arc basins, suggesting an important role for the upper plate in the deformation process [*Wells et al.*, 2003], although large events occur elsewhere along the Kuril zone where there is no prominent fore-arc basin, so no generalization emerges. TPGA indicates the degree to which the near-trench upper plate is out of isostatic equilibrium, which can be interpreted to delineate regions of elastic strain accumulation in the upper plate of subduction regimes during the interseismic period. If this

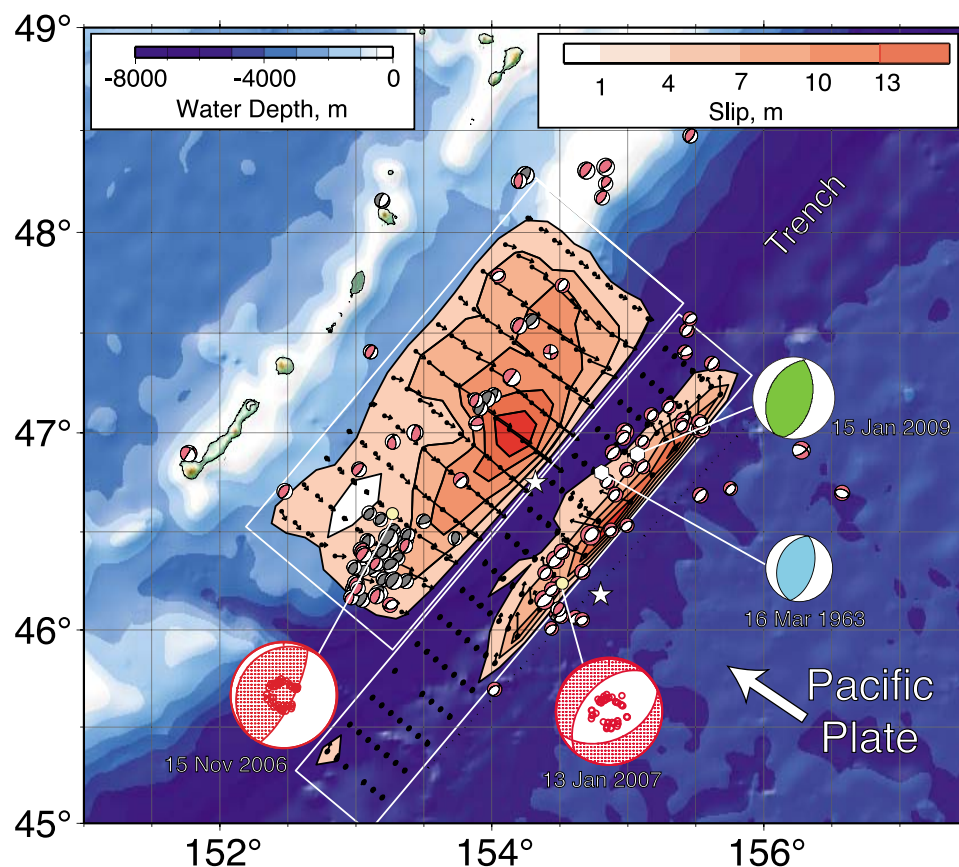


Figure 14. Surface map projection of coseismic slip for the 15 November 2006 (average slip 6.5 m) and the northwest dipping plane for 13 January 2007 (average slip 6.7 m at depths less than 25 km) events (NEIC epicenters, yellow circles, and CMT centroid epicenters, stars). Figure 15 indicates the relative position of the slip surfaces at depth. CMT mechanisms (centered on NEIC epicenters) for large events between June 2006 and May 2007 are shown; enlarged versions with first motions for the doublet events. Gray mechanisms indicate events before the 15 November 2006 event; red mechanisms indicate events after that rupture. The focal mechanism and epicenter of the 16 March 1963 (blue mechanism) and 15 January 2009 (green mechanism) compressional trench slope events (hexagons) are included. The arrow indicates the direction of the Pacific plate motion at 80 mm/yr.

holds for our region, it can be inferred that the upper plate near the 2006 event was less strained than might be expected given the size of the event, perhaps due to high strength of the upper plate or locally weak interplate coupling.

[42] Outer rise normal faulting occurs in most subduction zones and is generally attributed to plate bending stresses acting on the lithosphere as the slab deforms on approach to the trench [e.g., *Stauder*, 1968a, 1968b; *Liu and McNally*, 1993]. The zone of active shallow normal faulting associated with bending is usually about 50–100 km wide, and generally represents on the order of 1 Ma of deformation as the lithosphere moves through the region. Total normal fault offset on any fault in the trench slope and outer rise is typically less than ~ 100 m, so the faults are expected to be

relatively fresh compared to the megathrust. Outer rise compressional faulting tends to be less frequent than extensional faulting, and is typically at greater depths (25–50 km) than the extensional regime [e.g., *Seno and Yamanaka*, 1996]. This is also commonly attributed to bending of the plate, just as the complementary pattern of shallow compression and deep extension at intermediate depths is attributed to unbending. However, there is a major question about how compressional faulting can occur in what should be the high strength core of the lithosphere as predicted by viscoelastic yield strength models for plates [e.g., *Mueller et al.*, 1996a]. The ~ 15 –30 km depth separation between extensional and compressional domains is also less than expected given effective elastic plate thicknesses (~ 50 km

Table 3. Tsunami Modeling Results for 15 November 2006

Modeler	ϕ (deg)	δ (deg)	λ (deg)	S (km ²)	D (m)	μ (N/m ²)	M_0 (N m)
<i>Tanioka et al.</i> [2008]	220	25	96	200 × 80	4.8	4×10^{10}	3.1×10^{21}
<i>Fujii and Satake</i> [2008]	214	15	92	200 × 100	2.5	4×10^{10}	2.0×10^{21}
	214	8	92	200 × 100	3.1	4×10^{10}	2.5×10^{21}
<i>Rabinovich et al.</i> [2008]	220	15	varies	250 × 100	3.9	(4×10^{10})	3.9×10^{21}

Table 4. Tsunami Modeling Results for 13 January 2007

Modeler	ϕ (deg)	δ (deg)	λ (deg)	S (km ²)	D (m)	μ (N/m ²)	M_o (N m)	M_o^a (N m)	M_o^b (N m)
<i>Tanioka et al.</i> [2008]	220	37	−108	130 × 30	6.4	4×10^{10}	1.0×10^{21}	1.3×10^{21}	1.3×10^{21}
<i>Fujii and Satake</i> [2008]	215	45	−110	240 × 40	2.0	5×10^{10}	1.0×10^{21}	1.0×10^{21}	2.6×10^{21}
	42	58	−114	240 × 40	2.3	5×10^{10}	1.1×10^{21}	1.1×10^{21}	2.9×10^{21}
<i>Rabinovich et al.</i> [2008]	42	58	varies	170 × 50	4.5	(5×10^{10})	1.9×10^{21}	1.9×10^{21}	1.9×10^{21}

^aCorrected for $\mu = 5 \times 10^{10}$ N/m².

^bCorrected for deep-water effect ($\times 6.8/2.6$), after *Rabinovich et al.* [2008].

for 100 Ma lithosphere). Processes such as concentrations of fluids that give acute local strength reductions at depths below the elastic flexural neutral surface have been invoked to account for the deep compressional activity [e.g., *Seno and Yamanaka*, 1996]. It has also been suggested that viscoelastic plate deformation can result in more complex internal plate stress distributions than predicted by purely elastic models [*Mueller et al.*, 1996a], so intuitive oversimplification of the cause of deep thrusting in the outer rise may be misleading.

[43] *Christensen and Ruff* [1988] proposed that outer rise faulting is sensitive to stress perturbations associated with large underthrusting events in the adjacent subduction zone superimposed on plate bending stresses. When the interplate zone is frictionally locked, the outer rise may experience shallow compressional events, whereas shallow extensional faulting dominates after the interplate fault ruptures. This interaction may reveal important attributes of the stress state in the subduction zone [*Dmowska et al.*, 1988; *Liu and McNally*, 1993; *Taylor et al.*, 1996]. The fault planes activated in the outer rise are not usually well-resolved due to the moderate size of the events that occur there, but outer rise and trench slope compressional faulting is relatively infrequent. On the basis of some inelastic plate stress calculations, *Mueller et al.* [1996b] contest the viability of interplate coupling variations being controlling factors in outer rise compressional activity and argue that regional stress/strength heterogeneities must be responsible for the limited occurrence of compressional events. The close spatial proximity of the large 1963 compressional, 2007 extensional and 2009 compressional Kuril trench slope events is particularly interesting in this context, although it is important to keep in mind the relative tectonic significance of these events.

[44] The 13 January 2007 ($M_W = 8.1$) event is the third largest recorded normal faulting event seaward of a subduction zone, after the 1933 Sanriku, Japan ($M_W = 8.4$) [*Kanamori*, 1971] and 1977 Sumba, Indonesia ($M_W = 8.3$) [*Lynnes and Lay*, 1988] earthquakes. *Gamage et al.* [2009] demonstrate that extensional aftershock faulting persists to at least 20–25 km depth in the vicinity of the great 1933 Sanriku rupture with no nearby compressional events, while intraplate compressional events occur at depths of 30–45 km away from the source region. This suggests that a great outer rise normal faulting event can suppress the occurrence of nearby compressional events at shallow depths. Great normal-faulting events in the trench slope or outer rise are relatively rare, and the earlier great events are located seaward of weakly coupled megathrusts [e.g., *Kanamori*, 1971; *Lynnes and Lay*, 1988], with faults steeply dipping toward the trench, compatible with ‘detachment’ of the slab due to strong slab-pull stresses being efficiently

communicated to the outer rise. It is clear that the extensional 2007 event dominates the trench slope tectonic deformation, given its large slip and fault dimensions, with the 1963 and 2009 compressional events clearly being secondary tectonic processes. Still, there has not been a prior example of a large compressional faulting event occurring soon after and below a great extensional event prior to the recent Kuril sequence.

[45] The slip models from our body wave finite source inversions are shown in map view in Figure 14 and a schematic cross section is shown in Figure 15. The transition from relatively shallow intraplate compression near the trench slope prior to the 2006 megathrust event to shallow intraplate extension afterward is qualitatively consistent with the notion of outer rise stress modulation by varying interplate frictional stresses [*Christensen and Ruff*, 1988; *Lay et al.*, 1989; *Lin and Stein*, 2004; *Taylor et al.*, 1996]. The Kurile doublet provides the clearest example yet observed of a full temporal pattern through the seismic cycle from interseismic to coseismic to interseismic, and we seek to understand the specific nature of the intraplate stress modulation to constrain the process. Stress transfer occurred on multiple time scales. Initial intraplate activity seaward of the megathrust commenced within 40 min of the large thrust event, suggesting that dynamic and/or static stress transfer triggered events in a highly strained segment of the Pacific Plate. There was a 60 day delay before the great normal faulting event occurred and an additional 2 year delay before the deeper compressional faulting occurred on 15 January 2009 below the 2007 rupture zone. These specific event time separations are interesting, but caution is warranted when discussing their implications.

[46] Determining the details of the rapid stress change that occurred within the Pacific plate in response to slip along the megathrust is difficult; however characteristics of the great Kuril doublet sequence allow us to elucidate some aspects of the change. We do so using the slip estimates from our finite slip inversions, recognizing that the associated seismic moments are larger than long-period estimates by factors of 1.5–2, so slip values have at least comparable uncertainty. This uncertainty may represent model assumptions, differences in geometry, and bandwidth limitations, but it appears that any bias is similar for the doublet events (in both cases, our seismic moments are about 1.5 times larger than the CMT solution so we give a range based on this number), so the relative values are considered meaningful to first order.

[47] An average of ~ 4.3 – 6.5 m of slip occurred on the megathrust rupture surface at depths from 5 to 20 km during the November 2006 event. This slip reflects relative motion between the Pacific and North American plates along the interface, but our seismic modeling does not directly partition this total displacement (and the elastic shear strain

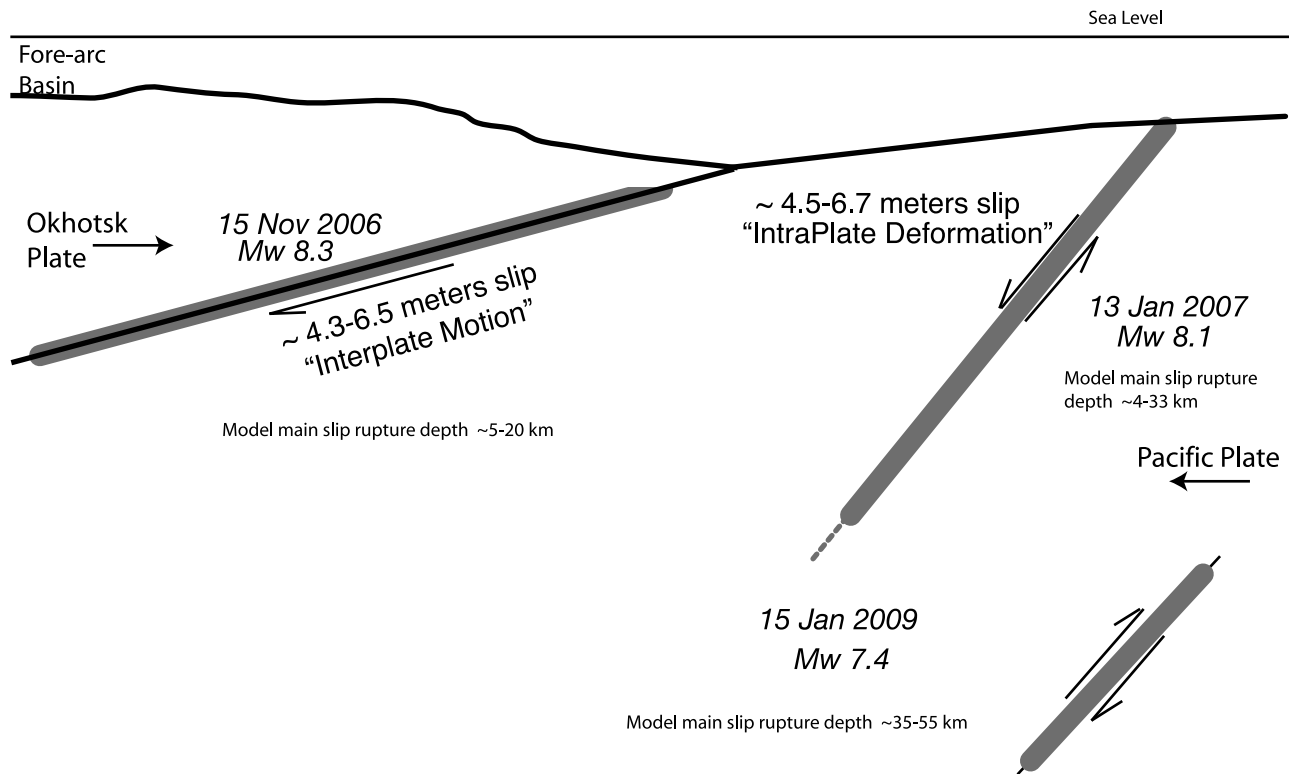


Figure 15. Schematic setting of the great Kuril Islands doublet events. The M_w 8.3, 15 November 2006, thrust-faulting earthquake ruptured the interface between the subducting Pacific and overriding North American (Okhotsk) plates, with approximately 4.3–6.5 m of average slip on the shallow portion of the megathrust above 25 km depth (broad line). The M_w 8.1, 13 January 2007 normal-faulting earthquake occurred within the Pacific plate beneath the trench slope region, with approximately 4.5–6.7 m of dip slip at (subseafloor) depths shallower than 25–30 km (broad line). Additional slip may have occurred beneath 30 km (dotted line). Resolved horizontal lengthening for either the northwestward dipping or southeastward dipping fault plane or the 2007 event is ~ 3.6 m. The 15 January 2009 compressional event occurred at depths below the extensional faulting region.

release it represents) between displacement of the subducting plate and overriding plate (relative to some far-field fixed reference). During 2006, approximately 5 months prior to the November 2006 event, a GPS network (comprised of both continuous GPS (cGPS) and episodic or survey mode GPS (eGPS) stations) was installed in the region [Steblov *et al.*, 2008]. Although this network (particularly the cGPS stations) provides information on the coseismic and postseismic deformation in the upper plate, only the cGPS sites provide constraints on the preearthquake strain accumulation. These sites are distant from the main rupture area, but do show a trend of decreasing displacement rates (from ~ 30 mm/yr to <10 mm/yr) (preearthquake) moving northeastward from Hokkaido and southwestward from Kamchatka toward the rupture area. This trend of decreasing shortening rates is consistent with the possibility of an upper plate with only moderate deformation along the local segment that ruptured in November 2006, perhaps also accounting for the absence of negative TPGA. Geodetic results from Japan [Takahashi and Kasahara, 2007] are too remote to provide much additional constraint. The January 2007 intraplate normal faulting event ruptured a steeply dipping fault, with coseismic slip concentrated in the upper 29 km of the Pacific lithosphere. The northwestward dipping fault plane (47° dip) with 4.5–6.7 m

of average dip slip leads to horizontal coseismic extension in the plate of 3.1–4.6 m. The southeastward dipping plane (59° dip, 5.1–7.7 m dip-slip displacement) produces approximately 2.6–3.9 m of horizontal extension. Allowing for the uncertainty in fault geometry there is $\sim 3.6 \pm 1.0$ m of plate lengthening in the 2007 event, about 75% of the underthrusting slip in the 2006 event. The Pacific plate lengthening could be attributed to bending stress extension that occurs after the megathrust induced compression is elastically relaxed, or to a direct measure of the interseismic compression relaxation, or some mixture of the two. We consider this question below.

[48] An attempt to quantify the Kuril doublet sequence is immediately confronted with our limited knowledge of the rheological properties of the plates, the relationship between earthquake activity and failure strength, and past history of the system. We outline the basic tectonic scenario (Figure 16) for the sequence, and then consider how differences in elastic versus anelastic behavior can lead to different implications of the faulting. The basic sequence is:

[49] 1. During the interseismic period, the shallow megathrust interface in the central Kuril Islands was locked and the motion between the Pacific and North American plates accommodated by strain within the two plates on either side of the locked thrust zone. A priori, how the strain

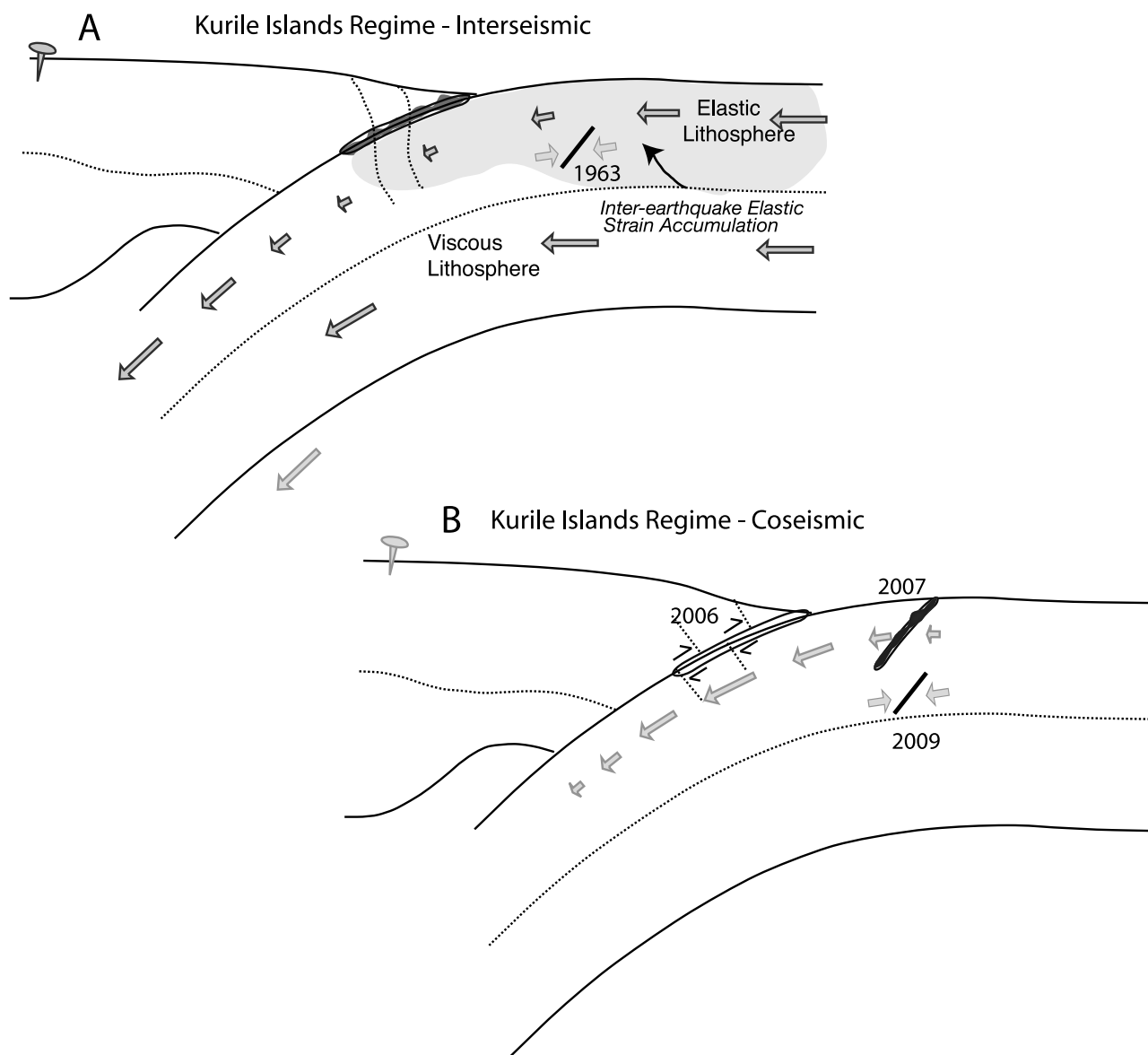


Figure 16. Strain accumulation and release scenario for the great Kuril doublet. (a) During the interseismic period, the Pacific–North America (Okhotsk) plate interface is locked along the megathrust. Because of relative strength contrast between subducting and overriding plates, the elastic strain may preferentially accumulate within the elastic layer of the Pacific plate. Below the elastic layer, viscous strain accommodates the deformation and there is along-strike loading by underthrusting of the adjacent region of the arc. (b) During the 2006 earthquake, slip along the megathrust interface allows that segment of the Pacific plate to recover the accumulated slip deficit, and relaxation of accumulated compression or slab pull places the updip shallow region into an extensional strain environment causing the great 2007 extensional event. The region at the elastic-ductile transition (dotted line) deforms by viscous processes during the low strain rate interearthquake period, but will behave elastically during the high strain rate underthrusting event, helping to delay strain release in the overlying elastic lithosphere.

partitioned between the subducting and overriding plates is hard to determine lacking sufficient geodetic measurements; arbitrary assumptions about this partitioning are commonly made, ranging from the strain being equally divided to the strain preferentially localizing within the (assumed) weaker accretionary margin of the upper plate. In the case of the 2006 Kurile event segment, the apparent lack of significant interseismic deformation of the upper plate given the absence of a gravitational anomaly and the lateral gradient

in prevent geodetic deformation along the arc implies that the elastic strain accumulation may have been preferentially (but not entirely) concentrated within the Pacific lithosphere. Interplate shear resistance combined with deep lithospheric and asthenospheric shear flow and lateral plate loading along the trench strike due to the great megathrust rupture in 1963 caused stress to build up in the trench slope regime. The 1963 compressional trench slope event represents this phase of accumulation of in-plane compressional

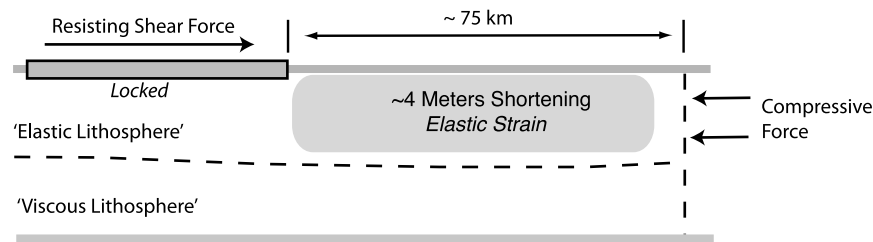


Figure 17. Configuration of the simple force balance used to estimate stress on the Pacific–North America (Okhotsk) megathrust interface under the assumption that the trench slope extensional faulting is associated with delayed strain release. The upper 25–30 km of the Pacific plate are assumed to deform elastically during the interearthquake period, effectively shortening by ~ 4 m. This strain is balanced by a compressive force provided by the trenchward displacement of the Pacific plate, shortening the plate against its locked boundary (the megathrust interface). That compressive force can be balanced against a component of the resisting shear stress along the megathrust.

stress, superimposed on any bending stress in the 25–35 km deep intraplate environment.

[50] 2. During the November 2006 event the megathrust slip removed a substantial portion or all of the slip deficit accumulated since the previous major event on that segment (1915?, 1780?).

[51] 3. The coseismic displacement of the Pacific plate along the megathrust released elastic shear stresses on the megathrust and at least some of the related stresses within the plate updip of the previously locked interface. This change in stress state led to the near-immediate onset of the extensive extensional earthquake activity outboard of the trench.

[52] 4. The great shallow January 2007 event results in ~ 4 m of horizontal extension of the upper portion of the Pacific plate in the plate motion direction.

[53] 5. The 45 km deep 15 January 2009 compressional event occurred below the region of the 2007 event. As shear strain slowly reaccumulated along the megathrust and as adjacent regions of the slab underthrust the arc, the compressional strain in the outer trench region will reaccumulate, enabling compressional events like that in 1963 to happen again in the future.

[54] This basic sequence has attributes that have different implications when viewed from purely elastic or viscoelastic perspectives. Perhaps of primary importance are the linked issues of timing of the two great earthquakes and their spatial relationship. The offshore normal faulting sequence initiates so quickly that elastic reduction of inhibiting compression was the likely trigger of the activity, however, the 2 month delay until the great 2007 event could be interpreted as a lower Pacific lithosphere viscous response along the lines of *Melosh's* [1976] interpretation of the 1965 Rat Island sequence.

[55] Other ways that the viscous properties of the deep lithosphere may influence the system are by localizing compressional strain in the Pacific plate updip of the megathrust during the interseismic period and then inhibiting relaxation of this compressional strain after the thrust event. It is possible that the region of compressively stressed Pacific lithosphere is defined by the extent of viscous relaxation that occurs during the interseismic period (100s of years). If we consider an end-member case in which all of the interplate slip deficit is accommodated by shortening

strain within the Pacific plate, then the Pacific plate must shorten at a rate of approximately 80 mm/yr. For an elastic model this shortening is distributed across the entire plate, but for a viscoelastic model the length-scale updip from the megathrust over which this shortening is accommodated can be controlled by the viscosity structure of the plate and the dimension of the interplate coupled zone. In a manner similar to the effects of viscous strain relaxation seen in the coupled elastic crust adjacent to major strike slip faults (assuming reasonable viscosities in the range of 3×10^{19} Pa s to 1×10^{20} Pa s) over periods of 50 to 200 years [e.g., *Malservisi et al.*, 2001], the extent of the highly strained zones is expected to be of order <100 km. Essentially, what is assumed to happen is that as the plate shortens, the lithosphere below the seismogenic layer deforms viscously, effectively localizing the elastic strain within the upper lithosphere to a region extending ~ 75 km updip of the locked zone. When the 2006 event occurs, shear strains in this region will relax coseismically, but to the extent that there is in-plane compressional strain that extends down to the viscous region, the short-term stiffness of that region can inhibit complete relaxation of the overlying compressional strain, possibly influencing the timing of the 2007 extensional faulting. As a viscoelastic process undergoing repeated loading and unloading of the interplate domain, the resultant stress and strain field may be complex in the trench slope region of the plate compared to the relatively simple perspective of elastic bending with superimposed in-plane compression/extension.

[56] Figure 17 shows a conceptual view of the interseismic compressional strain localization scenario where we ignore any contribution of background bending stresses. During the interseismic period, we assume that approximately 4 m of shortening is accommodated in an ~ 75 km wide zone updip of the locked thrust zone. This leads to a shortening strain of $\sim 5.6 \times 10^{-5}$. If this strain accumulates over 100 years then it reflects a strain rate of $\sim 1.5\text{--}2 \times 10^{-14}$ s $^{-1}$ ($4.8\text{--}6.4 \times 10^{-7}$ yr $^{-1}$) which is typical of plate boundary regions. We can relate this strain to the equivalent elastic stress that maintains it through the following:

$$\sigma_1 = \frac{(1 - \nu)E \varepsilon_1}{(1 + \nu)(1 - 2\nu)}$$

where $\nu = 0.25$ (Poisson's Ratio), and $E = 8 \times 10^{10}$ Pa (Young's Modulus). This leads to a compressive stress of $\sigma_1 = 5.1$ MPa. We can construct a simple force balance between the force necessary to produce this stress (and strain) with the 'frictional' or shear force acting along the locked plate interface (Figure 17). For a unit length along the strike of the plate boundary segment, and assuming an elastic thickness comparable to the rupture depth extent of the normal faulting event of 20–30 km, the equivalent force acting on the Pacific plate to shorten it by ~ 4 m over 75 km is between 1.0×10^{11} N and 1.5×10^{11} N or an average of $\sim 1.25 \times 10^{11}$ N. This force is balanced by a shear force resisting the downdip movement of the Pacific plate along the megathrust. This provides a lower bound of ~ 2 MPa of stress change on the 75–80 km wide coupled interplate fault. Uncertainty in how much strain released coseismically during the 2006 event and how much of the 2007 extensional faulting is actually releasing elastic bending stresses precludes imposing stronger constraints on the interplate coupling.

[57] While the occurrence of the 2009 compressional event ~ 30 km below the 2007 extensional event centroid is strongly suggestive of elastic bending effects, we acknowledge that it is difficult to reconcile these precise depths with conventional lithospheric strength notions without invoking ad hoc localized weakening processes. The similar locations of the 1963 and 2009 events do indicate that conditions that allow intraplate compressional faulting about 40 km deep existed both before and after the two great interplate events in a localized region of the plate. Given the complex stress regime that can develop in viscoelastic media over time, we cannot preclude an explanation independent of bending, but the consistency of depth for the compressional faulting in this region with that for many other regions argues for some common controlling factor such as bending stresses.

6. Conclusions

[58] The 2006–2007 Great Kuril earthquake sequence involved coupled underthrusting and extensional faulting on a large scale that has not been previously observed. The great thrust event of 15 November 2006 ruptured the shallow region of the megathrust fault between the Pacific plate and the Kuril arc, with ~ 4.3 – 6.5 m of slip along a ~ 250 km long segment of the boundary in what had been the central Kuril seismic gap. This event produced extensive aftershock activity along the megathrust as well as in the trench slope region, and two months later the 13 January 2007 normal-faulting event involved comparable amounts of slip on a steeply dipping intraplate fault near the trench. The region seaward of the megathrust had previously experienced a relatively shallow large compressional event (16 March 1963), so it appears that the shallow stress environment cycled from compression to extension with the stress release on the megathrust. Slip during the November 2006 event may have preferentially released elastic strain within the subducted Pacific slab, rather than having the strain release evenly partitioned between the subducted and overriding lithospheres, as is typically assumed but rarely documented. This asymmetry in strain release is suggested by the lack of a negative TPGA

anomaly in the region. The upper plate did experience some deformation, as evidenced by GPS observations. The efficient stress cycling and size of the events involved further suggests that complete loss of slip deficit on the megathrust may have allowed a near detachment-type extensional event to occur beneath the trench, similar to the large detachment events previously observed only in uncoupled seismic zones. A deep (45 km) compressional event in January 2009 occurred below the 2007 rupture zone, suggesting that bending forces were enhanced by slab pull when the megathrust decoupled. Alternatively, the great extensional faulting may be a viscoelastic manifestation of delayed relaxation of accumulated compressional strain in the plate updip of the megathrust, in which case it may provide a lower bound on the stress change on the megathrust. Such triggering of great intraplate faulting constitutes a hazard near subduction zones that has not been fully appreciated.

[59] **Acknowledgments.** We thank the developers of GMT and SAC and the global and transportable seismic network operators who have constructed a superb open data access network for seismic research and monitoring. Ed Gamero and Christine Houser provided algorithms used for computing spherical model travel time corrections for tomography models. We thank M. Raeesi and Y. Fujii for prepublication copies of their papers and Gavin Hayes, Daniel McNamara, and Phil Cummins for comments and discussions of the events. We thank Roland Bergmann and an anonymous reviewer for their helpful comments. The facilities of the IRIS Data Management System were used to access the data used in this study. Supported by NSF grants EAR0453884 and EAR0635570 (T.L.) and USGS Award 05HQGR0174 (C.J.A.).

References

- Abe, K. (1979), Size of great earthquakes of 1837–1974 inferred from tsunami data, *J. Geophys. Res.*, *84*, 1561–1568, doi:10.1029/JB084iB04p01561.
- Ammon, C. J., A. A. Velasco, and T. Lay (1993), Rapid estimation of rupture directivity: Application to the 1992 Landers ($M_S = 7.4$) and Cape Mendocino ($M_S = 7.2$) California earthquakes, *Geophys. Res. Lett.*, *20*, 97–100, doi:10.1029/92GL03032.
- Ammon, C. J., A. A. Velasco, and T. Lay (2006a), Rapid estimation of first-order rupture characteristics for large earthquakes using surface waves: 2004 Sumatra-Andaman earthquake, *Geophys. Res. Lett.*, *33*, L14314, doi:10.1029/2006GL026303.
- Ammon, C. J., H. Kanamori, T. Lay, and A. A. Velasco (2006b), The 17 July 2006 Java tsunami earthquake ($M_w = 7.8$), *Geophys. Res. Lett.*, *33*, L24308, doi:10.1029/2006GL028005.
- Ammon, C. J., H. Kanamori, and T. Lay (2008), A great earthquake doublet and seismic stress transfer cycle in the central Kuril islands, *Nature*, *451*, 561–566, doi:10.1038/nature06521.
- Apel, E. V., R. Bürgmann, G. Steblov, N. Vailenko, R. King, and A. Prytkov (2006), Independent active microplate tectonics of northeast Asia from GPS velocities and block modeling, *Geophys. Res. Lett.*, *33*, L11303, doi:10.1029/2006GL026077.
- Baba, T., P. R. Cummins, H. K. Thio, and H. Tsushima (2009), Validation and joint inversion of teleseismic waveforms for earthquake source models using deep ocean bottom pressure records: A case study of the 2006 Kuril megathrust earthquake, *Pure Appl. Geophys.*, *166*, 55–76, doi:10.1007/s00024-008-0438-1.
- Beck, S. L., and L. J. Ruff (1987), Rupture process of the great 1963 Kurile Islands earthquake sequence: Asperity interaction and multiple event rupture, *J. Geophys. Res.*, *92*, 14,123–14,138, doi:10.1029/JB092iB13p14123.
- Boschi, L., and G. Ekström (2002), New images of the Earth's upper mantle from measurements of surface wave phase velocity anomalies, *J. Geophys. Res.*, *107*(B4), 2059, doi:10.1029/2000JB000059.
- Christensen, D. H., and L. J. Ruff (1988), Seismic coupling and outer-rise earthquakes, *J. Geophys. Res.*, *93*, 13,421–13,444, doi:10.1029/JB093iB11p13421.
- De Mets, C., R. G. Gordon, D. F. Argus, and S. Stein (1990), Current plate motions, *Geophys. J. Int.*, *101*, 425–478, doi:10.1111/j.1365-246X.1990.tb06579.x.
- Dmowska, R., J. R. Rice, L. C. Lovison, and D. Josell (1988), Stress transfer and seismic phenomena in coupled subduction zones during

- the earthquake cycle, *J. Geophys. Res.*, *93*, 7869–7884, doi:10.1029/JB093iB07p07869.
- Dziwonski, A. M., and D. L. Anderson (1981), Preliminary reference Earth model, *Phys. Earth Planet. Inter.*, *25*, 297–356, doi:10.1016/0031-9201(81)90046-7.
- Fedotov, S. A. (1965), Regularities of the distribution of strong earthquakes in Kamchatka, the Kurile Islands, and northeastern Japan (in Russian), *Trudy Inst. Fiz. Zemli Akad. Nauk. SSSR*, *36*, 66–93.
- Fedotov, S. A. (1968), The seismic cycle, possibility of the quantitative seismic zoning, and long-term seismic forecasting, in *Seismic Zoning in the USSR*, edited by S. V. Medvedev, pp. 133–166, Nauka, Moscow.
- Fujii, Y., and K. Satake (2008), Tsunami sources of November 2006 and January 2007 great Kuril earthquakes, *Bull. Seismol. Soc. Am.*, *98*, 1559–1571, doi:10.1785/0120070221.
- Fukao, Y., and M. Furumoto (1979), Stress drops, wave spectra and recurrence intervals of great earthquakes—Implications of the Etorofu earthquake of 1958 November 6, *Geophys. J. R. Astron. Soc.*, *57*, 23–40.
- Gamage, S. S. N., N. Umino, A. Hasegawa, and S. H. Kirby (2009), Off-shore double-planned shallow seismic zone in the NE Japan forearc region revealed by sP depth phases recorded by regional networks, *Geophys. J. Int.*, *178*, 195–214, doi:10.1111/j.1365-246x.2009.04048.x.
- Geller, R. J., and H. Kanamori (1977), Magnitudes of great shallow earthquakes from 1904 to 1952, *Bull. Seismol. Soc. Am.*, *67*, 587–598.
- Grand, S. P. (2002), Mantle shear-wave tomography and the fate of subducted slabs, *Philos. Trans. R. Soc. London, Ser. A*, *360*, 2475–2491, doi:10.1098/rsta.2002.1077.
- Gutenberg, B., and C. F. Richter (1954), *Seismicity of the Earth and Associated Phenomena*, 2nd ed., 310 pp., Princeton Univ. Press, Princeton, N. J.
- Horrillo, J., W. Knight, and Z. Kowalik (2008), Kuril Islands tsunami of November 2006: 2. Impact at Crescent City by local enhancement, *J. Geophys. Res.*, *113*, C01021, doi:10.1029/2007JC004404.
- Houser, C., G. Masters, P. Shearer, and G. Laske (2008), Shear and compressional velocity models of the mantle from cluster analysis of long-period waveforms, *Geophys. J. Int.*, *174*, 195–212, doi:10.1111/j.1365-246X.2008.03763.x.
- Iida, K., D. C. Cox, and G. Paras-Carayannis (1967), Preliminary catalog of tsunamis occurring in the Pacific Ocean, *Data Rep. 5, HIG-67-10*, 261 pp., Hawaii Inst. of Geophys. Univ. of Hawaii, Honolulu.
- Ishii, M., P. M. Shearer, H. Houston, and J. E. Vidale (2005), Extent, duration and speed of the 2004 Sumatra-Andaman earthquake imaged by the Hi-net array, *Nature*, *435*, 933–936.
- Ishii, M., P. M. Shearer, H. Houston, and J. E. Vidale (2007), Teleseismic P-wave imaging of the 26 December 2004 Sumatra-Andaman and 28 March 2005 Sumatra earthquake ruptures using the Hi-net array, *J. Geophys. Res.*, *112*, B11307, doi:10.1029/2006JB004700.
- Johnson, J. M., and K. Satake (1999), Asperity distribution of the 1952 great Kamchatka earthquake and its relation to future earthquake potential in Kamchatka, *Pure Appl. Geophys.*, *154*, 541–553, doi:10.1007/s000240050243.
- Kagan, Y. Y., and D. D. Jackson (1999), Worldwide doublets of large shallow earthquakes, *Bull. Seismol. Soc. Am.*, *89*, 1147–1155.
- Kanamori, H. (1970), Synthesis of long-period surface waves and its application to earthquake source studies—Kuril Islands earthquake of October 13, 1963, *J. Geophys. Res.*, *75*, 5011–5027, doi:10.1029/JB075i026p05011.
- Kanamori, H. (1971), Seismological evidence for a lithospheric normal faulting: The Sanriku earthquake of 1933, *Phys. Earth Planet. Inter.*, *4*, 289–300, doi:10.1016/0031-9201(71)90013-6.
- Kanamori, H. (1976), Re-examination of the Earth's free oscillations excited by the Kamchatka earthquake of November 4, 1952, *Phys. Earth Planet. Inter.*, *11*, 216–226, doi:10.1016/0031-9201(76)90066-2.
- Kanamori, H. (1993), *W*-phase, *Geophys. Res. Lett.*, *20*, 1691–1694, doi:10.1029/93GL01883.
- Kanamori, H., and L. Rivera (2008), Source inversion of *W*-phase: Speeding up seismic tsunami warning, *Geophys. J. Int.*, *175*, 222–238, doi:10.1111/j.1365-246X.2008.03887.x.
- Kelleher, J., and W. McCann (1976), Buoyant zones, great earthquakes and unstable boundaries of subduction, *J. Geophys. Res.*, *81*, 4885–4896, doi:10.1029/JB081i026p04885.
- Kennett, B. L. N., and E. R. Engdahl (1991), Traveltimes for global earthquake location and phase identification - IASP91 model, *Geophys. J. Int.*, *105*, 429–465, doi:10.1111/j.1365-246X.1991.tb06724.x.
- Kikuchi, M., and H. Kanamori (1991), Inversion of complex body waves III, *Bull. Seismol. Soc. Am.*, *81*, 2335–2350.
- Kowalik, Z., J. Horillo, W. Knight, and T. Logan (2008), Kuril Islands tsunami of November 2006: I. Impact at Crescent City by distant scattering, *J. Geophys. Res.*, *113*, C01020, doi:10.1029/2007JC004402.
- Krüger, F., and M. Ohmberger (2005), Tracking the rupture of the $M_w = 9.3$ Sumatra earthquake over 1,150 km at teleseismic distance, *Nature*, *435*, 937–939, doi:10.1038/nature03696.
- Kulinich, R. G., B. Y. Karp, B. V. Baranov, E. P. Lelikov, V. N. Karnaukh, M. G. Valitov, S. M. Nikolaev, T. N. Kolpashchnikova, and I. B. Tsoi (2007), Structural and geological characteristics of a “seismic gap” in the central part of the Kuril Island arc, *Russ. J. Pac. Geol.*, *1*, 3–14, doi:10.1134/S1819714007010022.
- Laverov, N. P., S. S. Lappo, L. I. Lobkovsky, B. V. Baranov, R. G. Kulinich, and B. Y. Karp (2006), The Central Kuril “Gap”: Structure and seismic potential, *Dokl. Earth Sci.*, *409*, 787–790, doi:10.1134/S1028334X06050254.
- Lay, T., and H. Kanamori (1980), Earthquake doublets in the Solomon Islands, *Phys. Earth Planet. Inter.*, *21*, 283–304, doi:10.1016/0031-9201(80)90134-X.
- Lay, T., H. Kanamori, and L. Ruff (1982), The asperity model and the nature of large subduction zone earthquakes, *Earthquake Predict. Res.*, *1*, 3–71.
- Lay, T., L. Astiz, H. Kanamori, and D. H. Christensen (1989), Temporal variation of large intraplate earthquakes in coupled subduction zones, *Phys. Earth Planet. Inter.*, *54*, 258–312, doi:10.1016/0031-9201(89)90247-1.
- Levin, B. W., et al. (2008), Manifestations of the tsunami of November 15, 2006, on the central Kuril Islands and results of the runup heights modeling, *Dokl. Earth Sci.*, *419*, 335–338, doi:10.1134/S1028334X08020335.
- Lin, J., and R. S. Stein (2004), Stress triggering in thrust and subduction earthquakes and stress interaction between the southern San Andreas and nearby thrust and strike-slip faults, *J. Geophys. Res.*, *109*, B02303, doi:10.1029/2003JB002607.
- Liu, X., and K. C. McNally (1993), Quantitative estimates of interplate coupling inferred from outer-rise earthquakes, *Pure Appl. Geophys.*, *140*, 211–255, doi:10.1007/BF00879406.
- Llenos, A. L., and J. J. McGuire (2007), Influence of fore-arc structure on the extent of great subduction zone earthquakes, *J. Geophys. Res.*, *112*, B09301, doi:10.1029/2007JB004944.
- Lynnes, C. S., and T. Lay (1988), Source process of the great 1977 Sumba earthquake, *J. Geophys. Res.*, *93*, 13,407–13,420, doi:10.1029/JB093iB11p13407.
- MacInnes, B. T., J. Bourgeois, T. K. Pinegina, M. E. Martin, and E. A. Kravchunovskaya (2007), Tsunami erosion: Geomorphology before and after the 15 Nov 2006 tsunami in the middle Kuril Islands, Russia, *Eos Trans. AGU*, *88*(52), Fall Meet. Suppl., Abstract OS31A-0158.
- Malservisi, R., K. P. Furlong, and T. H. Dixon (2001), Influence of the earthquake cycle and lithospheric rheology on the dynamics of the eastern California shear zone, *Geophys. Res. Lett.*, *28*, 2731–2734, doi:10.1029/2001GL013311.
- McCann, W. R., S. P. Nishenko, L. R. Sykes, and J. Krause (1979), Seismic gaps and plate tectonics: Seismic potential for major boundaries, *Pure Appl. Geophys.*, *117*, 1082–1147, doi:10.1007/BF00876211.
- Mégnin, C., and B. Romanowicz (2000), The three-dimensional shear velocity structure of the mantle from the inversion of body, surface, and higher-mode waveforms, *Geophys. J. Int.*, *143*, 709–728, doi:10.1046/j.1365-246X.2000.00298.x.
- Melosh, H. J. (1976), Nonlinear stress propagation in the Earth's upper mantle, *J. Geophys. Res.*, *81*, 5621–5632, doi:10.1029/JB081i032p05621.
- Mueller, S., W. Spence, and G. L. Choy (1996a), Inelastic models of lithospheric stress - I. Theory and application to outer-rise plate deformation, *Geophys. J. Int.*, *125*, 39–53, doi:10.1111/j.1365-246X.1996.tb06533.x.
- Mueller, S., W. Spence, and G. L. Choy (1996b), Inelastic models of lithospheric stress - II. Implications for outer-rise seismicity and dynamics, *Geophys. J. Int.*, *125*, 54–72, doi:10.1111/j.1365-246X.1996.tb06534.x.
- Ni, S., H. Kanamori, and D. Helmberger (2005), Energy radiation from the Sumatra earthquake, *Nature*, *434*, 582, doi:10.1038/434582a.
- Nishenko, S. P. (1991), Circum-Pacific seismic potential 1989–1999, *Pure Appl. Geophys.*, *135*, 169–259, doi:10.1007/BF00880240.
- Norimatsu, K., and J. J. Mori (2008), Fault plane determination and possible triggering of the 2007 Kuril Island earthquake (M_w 8.1), *Eos Trans. AGU*, *89*(53), Fall Meeting Suppl., Abstract S23B-1886.
- Pacheco, J. F., and L. R. Sykes (1992), Seismic moment catalog of large shallow earthquakes, 1900 to 1989, *Bull. Seismol. Soc. Am.*, *8*, 1306–1349.
- Perez, O. J. (2000), Kuril Islands Arc: Two seismic cycles of great earthquakes during which the complete history of seismicity ($M_S \geq 6$) is observed, *Bull. Seismol. Soc. Am.*, *90*, 1096–1100, doi:10.1785/0119990063.
- Pinegina, T., J. Bourgeois, B. MacInnes, E. Kravchunovskaya, M. E. Martin, and N. Razhegaeva (2007), Paleotsunamis in the Middle Kuril Islands—Implications for a seismic gap (and in view of recent events), *Eos Trans. AGU*, *88*(52), Fall Meet. Suppl., Abstract OS31A-0161.
- Rabinovich, A. B., L. I. Lobkovsky, I. V. Fine, R. E. Thomson, T. N. Ivelskaya, and E. A. Kulikov (2008), Near-source observations and modeling of the Kuril Islands tsunamis of 15 November 2006 and 13 January 2007, *Adv. Geosci.*, *14*, 105–116.

- Raeesi, M., and K. Atakan (2009), On the deformation cycle of a strongly coupled plate interface: The triple earthquakes of 16 March 1963, 15 November 2006, and 13 January 2007 along the Kurile subduction zone, *J. Geophys. Res.*, *114*, B10301, doi:10.1029/2008JB006184.
- Seno, T., and Y. Yamanaka (1996), Double seismic zones, compressional deep trench-outer rise events, and superplumes, in *Subduction: Top to Bottom*, *Geophys. Monogr. Ser.*, vol. 96, edited by G. E. Bebout et al., pp. 347–355, AGU, Washington, D. C.
- Solov'ev, S. L., and M. D. Ferchev (1961), Summary of data on tsunamis in the USSR (in Russian), *Bull. Counc. Seismol.*, *9*, 1–37. (English translation by W. G. Van Campen, Hawaii Inst. Geophys. Transl. Ser., vol. 9.)
- Song, T. A., and M. Simons (2003), Large trench-parallel gravity variations predict seismogenic behavior in subduction zones, *Science*, *301*, 630–633, doi:10.1126/science.1085557.
- Stauder, W. (1968a), Mechanism of the Rat Island earthquake sequence of February 4, 1965 with relation to island arcs and sea-floor spreading, *J. Geophys. Res.*, *73*, 3847–3858, doi:10.1029/JB073i012p03847.
- Stauder, W. (1968b), Tensional character of earthquake foci beneath the Aleutian trench with relation to sea-floor spreading, *J. Geophys. Res.*, *73*, 7693–7701, doi:10.1029/JB073i024p07693.
- Steblov, G. M., M. G. Kogan, B. V. Levin, N. F. Vasilenko, A. S. Prytkov, and D. I. Frolov (2008), Spatially linked asperities of the 2006–2007 great Kuril earthquakes revealed by GPS, *Geophys. Res. Lett.*, *35*, L22306, doi:10.1029/2008GL035572.
- Takahashi, H., and M. Kasahara (2007), Geodetic constraint on the slip distribution of the 2006 Central Kuril earthquake, *Earth Planets Space*, *59*, 1095–1098.
- Tanioka, Y., Y. Hasegawa, and T. Kuwayama (2008), Tsunami waveform analysis of the 2006 underthrust and 2007 outer-rise Kurile earthquakes, *Adv. Geosci.*, *14*, 129–134.
- Taylor, M. A. J., G. Zheng, J. R. Rice, W. D. Stuart, and R. Dmowska (1996), Cyclic stressing and seismicity at strong coupled subduction zones, *J. Geophys. Res.*, *101*, 8363–8381, doi:10.1029/95JB03561.
- Velasco, A. A., C. J. Ammon, and S. L. Beck (2000), Broadband source modeling of the November 8, 1997, Tibet ($M_w = 7.5$) earthquake and its tectonic implications, *J. Geophys. Res.*, *105*, 28,065–28,080, doi:10.1029/2000JB900282.
- Walck, M. C. (1984), The *P*-wave upper mantle structure beneath an active spreading center; the Gulf of California, *Geophys. J. R. Astron. Soc.*, *76*, 697–723.
- Walker, K. T., M. Ishii, and P. M. Shearer (2005), Rupture details of the 28 March 2005 Sumatra M_w 8.6 earthquake imaged with teleseismic *P*-waves, *Geophys. Res. Lett.*, *32*, L24303, doi:10.1029/2005GL024395.
- Wells, R. E., R. J. Blakely, Y. Sugiyama, D. W. Scholl, and P. A. Dinterman (2003), Basin-centered asperities in great subduction zone earthquakes: A link between slip, subsidence, and subduction erosion?, *J. Geophys. Res.*, *108*(B10), 2507, doi:10.1029/2002JB002072.
- Xu, X., K. D. Koper, O. Sufri, L. Zhu, and A. R. Hutko (2009), Rupture imaging of the M_w 7.9 May 12, 2008 Wenchuan earthquake from back projection of teleseismic *P* waves, *Geochem. Geophys. Geosyst.*, *10*, Q04006, doi:10.1029/2008GC002335.
- Zheng, Y., and T. Lay (2006), Low V_p/V_s ratios in the crust and upper mantle beneath the Sea of Okhotsk inferred from teleseismic p_mP , s_mP , and s_mS underside reflections from the Moho, *J. Geophys. Res.*, *111*, B01305, doi:10.1029/2005JB003724.

C. J. Ammon and K. Furlong, Department of Geosciences, Pennsylvania State University, 440 Deike Bldg., University Park, PA 16802-0000, USA.

A. R. Hutko, U.S. Geological Survey, NEIC, MS 966, Box 2504, DFC, Denver, CO 80225-0000, USA.

H. Kanamori, Seismological Laboratory, California Institute of Technology, 1200 East California Blvd., Pasadena, CA 91125-0000, USA.

T. Lay, Department of Earth and Planetary Sciences, University of California, Santa Cruz, 1156 High St., Earth and Marine Sciences Bldg., Santa Cruz, CA 95064, USA. (thorne@pmc.ucsc.edu)

L. Rivera, Institut de Physique du Globe de Strasbourg, 5 rue Rene Descartes, F-67084 Strasbourg, France.